

Enhanced Water Flow through Carbon Nanotubes:
Using Computer Simulation to Identify the Governing
Mechanisms and Explore the Associated Heat Transfer

A thesis proposal by
John A. Thomas

February 11, 2008
224 Scaife Hall
Department of Mechanical Engineering
Carnegie Mellon University

Thesis Committee

Dr. Alan McGaughey, Committee Chair and Assistant Professor of Mechanical Engineering
Dr. Shelley Anna, Assistant Professor of Mechanical Engineering
Dr. Nadine Aubry, Professor and Department Head of Mechanical Engineering
Dr. Mohammed Islam, Assistant Professor of Chemical Engineering

Contents

I Thesis Overview	3
A Introduction	3
B Objectives	5
II Flow and Heat Transfer: From the Continuum to the Nanoscale	6
A Fluid Flow	6
B Thermal Energy Transport	8
III Molecular Dynamics Simulation	13
A Introduction and Overview	13
B Intermolecular Potential Functions	13
C Data Collection	16
IV Proposed Research and Preliminary Findings	20
A Identify the Mechanisms Responsible for Enhanced Water Flow in CNTs . .	20
B Examine Heat Transfer to the Confined Fluid	24
C Improve the Water/CNT Intermolecular Potential	26
V Outcomes and Schedule	31
VI Biographical Sketch	32
VIII References	33

I. Thesis Overview

A. Introduction

Advances in carbon nanotube (CNT) fabrication techniques and new experimental and theoretical investigations into fluid flow through ultra-confined geometries have generated interest in nanofluidic-based sensors and devices.¹ Yun *et al.* recently fabricated stable and axially-aligned CNT arrays with an unprecedented length of 1 cm.² Li *et al.* built CNT networks containing well-aligned and uniform CNT Y-junctions with controllable branch and spur dimensions.³ Shim *et al.* functionalized CNT surfaces to be biocompatible and capable of recognizing proteins.⁴ Moreover, multiple research groups have fabricated CNT membranes with tailored tube diameters and lengths using fabrication procedures easily scalable to large surface areas.^{5,6}

In addition to these new fabrication capabilities, laboratory experiments have demonstrated that the permeability of gases through CNT membranes is 10 to 100 times greater than would be predicted using conventional Knudsen permeability theory.⁷ This enhancement is caused by (i) the atomistically smooth tube surface, which interacts elastically with gas molecules, and (ii) the non-uniform distribution of gas molecules across the CNT cross-section, which reduces flow friction.⁸ Having identified the mechanisms responsible the enhanced flow, Sholl and co-workers developed a gas/membrane permeability model based on the gas density profile, CNT geometry, and membrane porosity.⁸

Experiments have also demonstrated that liquid water travels almost friction-free through sub-10 nm diameter CNTs. In monitoring water flow through a membrane of aligned 7 nm diameter CNTs, Majumder *et al.* measured flow rates four to five *orders of magnitude* greater than would be predicted from the continuum-based no-slip Hagen-Poiseuille relation.⁶ Holt *et al.*, who constructed a CNT membrane with tube diameters ranging from 1.3 to 2.0 nm, observed similar high water flow rates which were two to four orders of magnitude larger than the values predicted using the same theory.⁵ Unlike gas flow, however, the mechanisms responsible for the enhanced water flow have not yet been elucidated and a model for the enhanced water flow through CNTs is not yet available.

There are a number of potential applications for custom engineered, high mass flow rate nanofluidic systems. Such devices closely mimic protein channels and are ideally suited for transdermal drug delivery and intercellular liquid transport.⁶ These high-permeability membranes may also allow for lower-energy industrial gas separation processes and low-cost molecular sieving.⁹ For use in water purification, CNT membranes could reduce by 75% the costs associated with desalination (currently about 0.50 US\$/m³).⁹ The ability to

sequester and transport individual molecules may also lead to precise chemical detection devices requiring small sample volumes.

The anomalously high flow rates suggest that energy exchange between fluid confined inside a CNT and the surrounding environment is unlike continuum descriptions of conduction and convection heat transfer. Instead, the nearly frictionless flow, which is characteristic of weak interactions between the solid and the liquid, implies that fluid inside the CNT will be thermally isolated from its surroundings.¹⁰ Experimental measurements have confirmed that heat transfer from a single-walled CNT to a surrounding polymer melt is limited by a very large thermal resistance across the solid-liquid boundary.¹¹ Computer simulations of similar systems show that this CNT/polymer melt interface resistance is a tunable parameter dependant on the tube geometry.¹² However, a systematic investigation into heat transfer to water confined inside CNTs, and how such energy exchange is affected by tube geometry, has yet to be performed.

The mass and heat transfer properties of such water/CNT systems—information necessary for nanofluidic device design and optimization—are related to (i) the water/carbon intermolecular potential, and (ii) the thermophysical properties of the confined liquid (which may be geometry dependent). Ideally, we would like to experimentally observe/measure the heat and mass transport phenomena/fluid properties. However, the very small length and time scales associated with non-continuum nanoscale transport phenomena make experimental measurements of such systems very difficult. Computer-based molecular dynamics (MD) simulation has emerged as a powerful tool for studying the behavior of many different solids, liquids, and gases over a range of length scales (1 Å to 1 μm), time scales (1 fs to 0.1 μs), and temperatures (0 K to 1000 K).^{13–16} In an MD simulation, particles are treated as rigid objects interacting via classical adaptations of quantum mechanical-based intermolecular potential functions. This ability to model individual molecular interactions, coupled with the ability to study transport at a variety of scales, makes MD simulation an ideal tool for studying water flow through nanofluidic systems and heat transfer across the water/CNT interface.

Accurate intermolecular potential functions, which are constructed using experimental data or information from electronic structure calculations, must be specified when performing an MD simulation of water/CNT systems. The water/water and carbon/carbon intermolecular potentials currently available have been used to reproduce several experimentally observed transport phenomena and material properties.^{17–19} The most accurate water/carbon intermolecular potential, which is based on the experimentally observed behavior of water droplets on graphene, is currently used to model interactions between water molecules and CNTs. However, since both the relative positions and electronic structure of atoms on the

carbon surface are affected by surface curvature,²⁰ the applicability of the water/graphite potential to water/CNT systems is questionable. Developing an intermolecular potential function specific to water/CNT interactions, which properly incorporates the effects of surface curvature, will increase the predictive capabilities of MD and more accurately reveal the heat and mass transfer mechanisms within nanofluidic systems.

B. Objectives

The objectives of the proposed research are to

1. Identify the fundamental physical mechanisms responsible for enhanced flow in sub-10 nm diameter CNTs,
2. Elucidate the nature of heat transfer between fluids inside and outside the tube and across the CNT surface, and
3. Develop an improved water/CNT interaction potential.

Electronic structure calculations, molecular dynamics simulation, and formulations grounded in statistical mechanics will be the primary tools used throughout the proposed research. From these findings, I will identify how the properties of the nanofluidic system (e.g. CNT diameter, applied pressure gradient, etc.) should be tailored to generate desired mass and heat transfer behavior. This information will be useful to engineers seeking to design systems that utilize the unique transport phenomena manifest at the nanoscale, and experimentalists who seek to understand heat transfer between CNTs and more complicated fluids and gels.²¹

II. Flow and Heat Transfer: From the Continuum to the Nanoscale

A. Fluid Flow

When subject to a pressure gradient, $\partial P/\partial z$, the volumetric flow rate, Q_{HP} , of incompressible laminar liquid flowing steadily through a macroscopic tube of diameter d is given by the Hagen-Poiseuille (HP) relation:

$$Q_{\text{HP}} = \frac{\pi (d/2)^4}{8\mu} \frac{\partial P}{\partial z}, \quad (1)$$

where μ is the absolute viscosity. These variables are assumed to be independent (e.g. the water viscosity is not a function of flow geometry), making the volumetric flow rate a function of the flow geometry, fluid properties, and applied pressure gradient. In deriving Eq. (1), the velocity of the fluid adjacent to the fixed solid surface is assumed to have zero velocity. This is the so-called “no-slip” boundary condition. The radial velocity profile, $u(r)$, for no-slip pressure-driven water flow inside a circular tube is then given by:

$$u(r) = 2\bar{V}_{\text{ns}} \left[1 - \frac{r^2}{R_s^2} \right]. \quad (2)$$

In Eq. (2), r is the radial position with respect to the tube centerline, R_s is the tube radius, and \bar{V}_{ns} is the average velocity:

$$\bar{V}_{\text{ns}} = \frac{\pi R_s^2}{8\mu} \frac{\partial P}{\partial z}. \quad (3)$$

Exceptions to the no-slip condition have been observed experimentally²² and predicted from computer simulation of confined fluid flow.¹⁰ Fluids are instead observed to “slip” across the solid surface with a velocity different from that of the boundary. As presented in Fig. 1(a) and (b), this velocity discontinuity can be described in terms of a slip length, L_s , defined as

$$L_s = \left. \frac{u(r)}{du/dr} \right|_{r=R_s}. \quad (4)$$

The velocity and the velocity gradient, du/dr , in Eq. (4) are to be evaluated at the liquid/solid boundary, where $r = R_s$. The Hagen-Poiseuille relation presented in Eq. (1) can be recast to include the effects of slip,

$$Q_{\text{HP}} = \frac{\pi [(d/2)^4 + (d/2)^3 L_s]}{8\mu} \frac{\partial P}{\partial z}. \quad (5)$$

The form of Eq. (5) agrees with intuition: larger slip lengths increase the flow rate through the tube, while a slip length of zero (the no-slip condition) recovers Eq. (1). The velocity

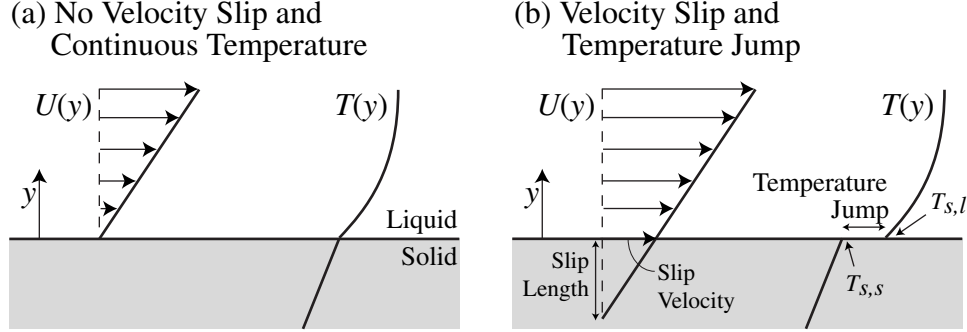


Figure 1: (a) Flat solid-liquid interface with no slip and no Kapitza resistance. (b) Flat solid-liquid interface with both slip and Kapitza resistance. In both figures, y is the position above the flat surface, $U(y)$ is the velocity profile, and $T(y)$ is the temperature profile. In cylindrical pipes, the velocity and temperature profiles are functions of radial position, r , relative to the tube centerline.

profile presented in Eq. (2) can also be modified to include the effects of slip:

$$u(r) = 2\bar{V}_{ns} \left[1 - \frac{r^2}{R_s^2} + 2\zeta \right], \quad (6)$$

where $\zeta = L_s/R_s$ is the ratio of slip length to tube radius, and \bar{V}_{ns} is the average velocity of the no-slip flow given by Eq. (3). For a no-slip system (i.e. $\zeta = 0$), we recover Eq. (2)

Typical slip lengths range from 5 nm in wetting systems to 35 nm in non-wetting systems.^{23,24} In macroscopic tubes with diameters greater than 1 mm, as shown in Figs. 2(a) and (b), such small slip lengths generate only a 0.01% to 0.001% enhancement to the total flow rate. Similarly, since ζ for macroscopic tubes is very close to zero, slip has no detectable effect on the velocity profile. For these reasons, slip is often neglected in macroscale applications. In microfluidic applications, where the characteristic dimension of the flow geometry is between 1 μm and 1 mm, slip has a more meaningful effect on the volumetric flow rate and axial velocity profile. For example, a 10 nm slip length in a 1 μm diameter tube will enhance the volumetric flow rate by 2% and increase the centerline velocity by 4%.

In nanofluidic applications, such as water flow through CNTs, the applicability of the slip-modified Hagen-Poiseuille relation is questionable. As shown in Fig. 2(a), even modified for slip, the model under-predicts the two experimentally-observed volumetric water flow rates by several orders of magnitude. Moreover, within such nanofluidic systems, the slip length may be larger than the tube itself, meaning the flow profile is essentially uniform across the tube cross section. Such behavior calls into question the assumed parabolic form of the velocity profiles and makes dubious the applicability of a slip-based correction to Hagen-Poiseuille formulation.⁸ Additionally, unlike in macro and microfluidic systems, where the water viscosity is independent of tube diameter, the thermophysical properties of

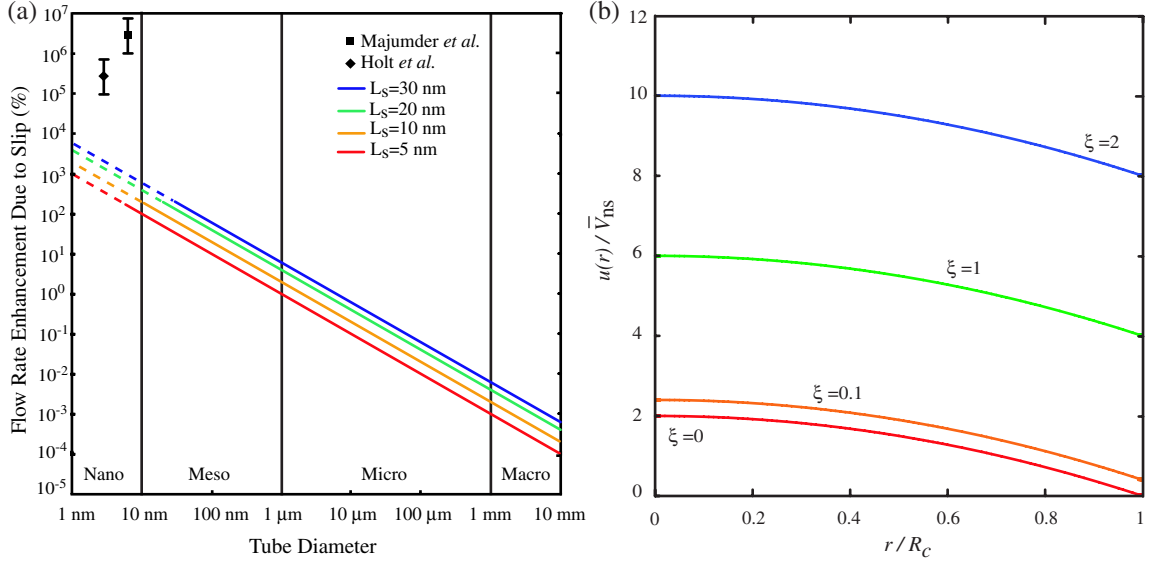


Figure 2: Enhancement to volumetric flow rate due to slip. The experimental data of Majumder *et al.*⁶ and Holt *et al.*⁵ is shown for comparison. The dashed lines indicate regions where the slip length is greater than the tube diameter.

fluids confined within sub-10 nm diameter CNTs are a function of tube diameter.^{25–27}

Two mechanisms to explain the fast transport behavior in CNTs have been proposed: (i) a breakdown of the hydrogen bonding network and (ii) reduced “friction” between the water molecules and the CNT surface. These arguments are heuristic; there is no quantitative understanding of how tube diameter influences either liquid structure or how the solid/liquid interaction is affected by surface curvature. However, such non-continuum effects—which necessitate modeling individual molecules and molecular interactions—are likely responsible for the enhanced flow inside CNTs. A clear and quantified description of the molecular interactions inside CNTs, and how these interactions change with CNT diameter, must be available before large-scale implementation and nanofluidic device design can begin.

B. Thermal Energy Transport

We now discuss heat transfer from a hot circular tube to a colder confined flowing fluid. Consider Newton’s law of cooling,

$$q''_s = h(T_{s,l} - T_m). \quad (7)$$

In Eq. (7), q'' is the heat flux from the solid to the liquid, h is the convection conductance, $T_{s,l}$ is the temperature of the adjacent surface (the meaning of the s, l subscript is discussed

below), and T_m is the mean fluid temperature given by

$$T_m = \frac{1}{\bar{V}_{ns} A_C} \int_{A_c} u(r) T(r) dA_c, \quad (8)$$

where A_C is the flow area cross-section, and $T(r)$ is the radial temperature profile in the fluid. The thermal conductivity of the fluid, k , is defined by the Fourier Law,

$$q_s'' = -k \left(\frac{\partial T}{\partial r} \right)_{r=R_s}. \quad (9)$$

Combining Eqs. (7) and (9) yields

$$\frac{h}{k} = \frac{\left(\frac{\partial T}{\partial r} \right)_{r=R_s}}{(T_{s,l} - T_m)}. \quad (10)$$

Equation (10) can be non-dimensionalized by multiplying both sides by the tube diameter $D (= 2R_s)$, such that

$$\frac{hD}{k} = \frac{\left(\frac{\partial T}{\partial r} \right)_{r=r_s}}{\frac{(T_{s,l} - T_m)}{D}} \equiv \text{Nu}. \quad (11)$$

This ratio is called the Nusselt number. It compares the temperature gradient of the fluid at the surface to an overall temperature difference, and is a ratio of the fluid conductive thermal resistance to the fluid convective thermal resistance. The Nusselt number describes the amount of heat transferred across the solid-liquid boundary, independent of the flow geometry and working fluid properties.

With a constant wall heat-flux, assuming a no-slip condition and assuming a fully-developed parabolic (i.e. laminar) velocity profile, Eqs. (7) to (11) can be combined to give $\text{Nu} = 4.36$. This prediction is in good agreement with experimental measurements.²⁸ Nusselt number correlations for systems with constant tube temperature, non-circular tube cross sections, the flow entry region, annular flow, and other more complex systems are available in the literature.^{7,29}

The presence of slip at the solid-liquid interface affects the Nusselt number. Using the slip-modified velocity profile presented in Eq. (6), and assuming a uniform wall heat flux, the Nusselt number can be approximated by

$$\text{Nu}(\zeta) \approx \frac{48}{11 - \zeta + \zeta^2}. \quad (12)$$

where, once again, ζ is the ratio of slip length to tube diameter. Equation (12) is plotted in Fig. 3 for four typical slip lengths. Note that in tubes with diameters greater than than $1 \mu\text{m}$, the effects of slip on the Nusselt number are negligible. Even with a 35 nm slip length, the

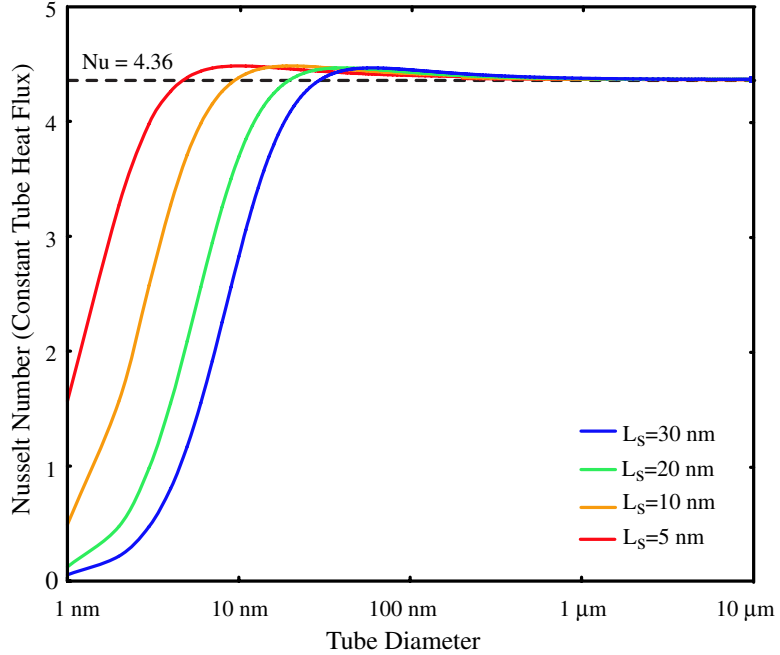


Figure 3: Effect of slip on Nusselt number for a circular pipe with constant wall heat flux.

Nusselt number in a $1 \mu\text{m}$ diameter tube is within 1% of the no-slip value. Thus, although slip enhances the flow rate, in this case the effects on the heat transfer are quite small.

Within the nanofluidic regime, the effects of slip on the Nusselt become more prevalent. If we assume the flow to be parabolic, a 20 nm slip length in a 10 nm tube reduces the Nusselt number to 3.68. A 30 nm slip length further reduces the Nusselt number to 2.82. As with the discussion of fluid flow, the validity of assuming a parabolic profile flow and the applicability of a slip-based correction to the flow are unclear within such small tubes. However, the low Nusselt numbers foreshadowed by slip-modified Hagen-Poiseuille flow model illustrate exciting possibilities of passive thermal insulation and ultra-low heat transfer fluid mechanical devices.

The $T_{s,l}$ symbol used above describes the temperature of the liquid directly adjacent to the solid surface. Both experiment³⁰ and simulation³¹ have demonstrated that a temperature discontinuity may exist at the solid-liquid interface, as depicted in Fig. 1(b). This temperature discontinuity is a manifestation of the Kapitza resistance across the interface, and is caused by weak thermal coupling between the solid and the liquid. If the symbol $T_{s,s}$ is used to describe the temperature on the solid-side of the interface, the Kapitza resistance, R_k , is then defined by

$$R_k = \frac{T_{s,s} - T_{s,l}}{q''}. \quad (13)$$

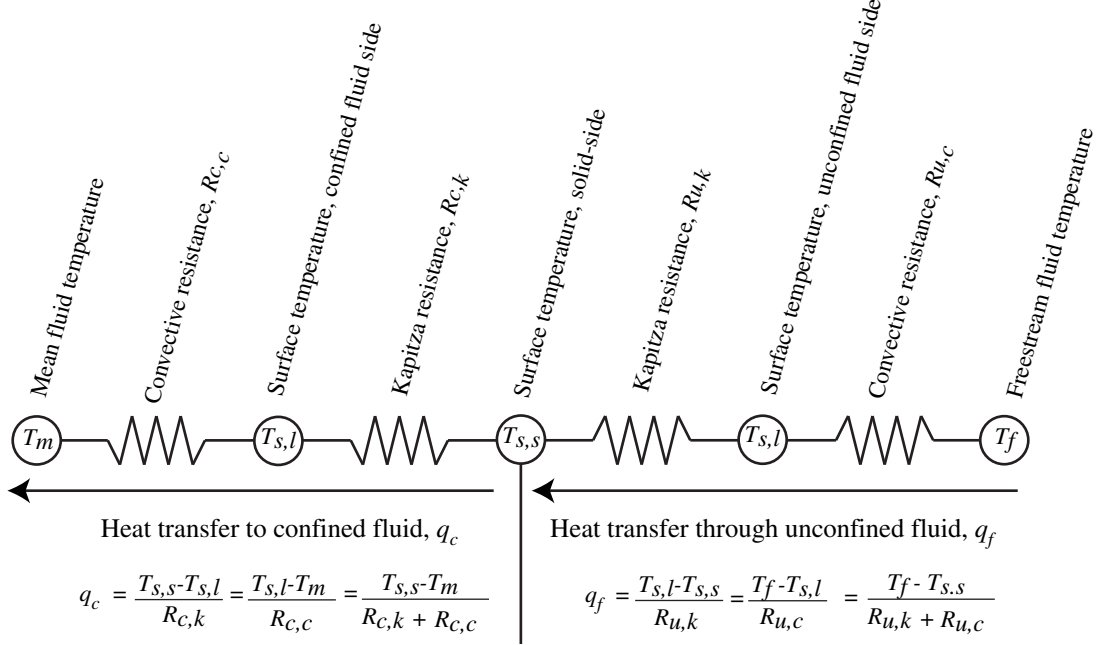


Figure 4: Thermal circuit description of heat transfer from an unconfined fluid, across the solid/liquid interface, and into the confined fluid. Understanding how both the convective thermal resistance and the Kapitza resistance vary with tube diameter is the clearest way to identify the effect of CNT geometry on thermal transport.

The Kapitza resistance can also be expressed in terms of a Kapitza length,

$$L_k = \left. \frac{T_{s,s} - T_{s,l}}{dT/dr} \right|_{R_s}. \quad (14)$$

Note that the Kapitza resistance is analogous to the slip phenomenon discussed previously. Their definitions, as presented in Eqs. (4) and (14), have similar forms and each phenomena describes a breakdown in transport across the solid-liquid boundary. This analogy between Kapitza resistance and slip was noted by Barrat and Chiaruttini,¹⁰ who report that systems with large slip lengths also have large Kapitza lengths.

Heat transfer from a fluid outside the CNT to a fluid confined inside the tube can be summarized using the thermal circuit diagram presented in Fig. 4. For a system with a fixed temperature difference, $(T_f - T_m)$, heat transfer to the confined fluid can be reduced by increasing the confined fluid convective resistance, $R_{c,c}$, the confined fluid/CNT Kapitza resistance, $R_{c,k}$, the unconfined fluid/CNT Kapitza resistance, $R_{u,k}$, or the unconfined fluid convective resistance, $R_{u,c}$. If either the confined or unconfined fluid is at rest with negligible natural convection, the convective thermal resistance is replaced by a conductive thermal resistance. Just like the convective resistance, increasing the conductive resistance decreases

the amount of heat transferred to the confined fluid. However, unlike the convective resistance which depends on the nature of flow, the conductive resistance is only a function of the fluid conductivity and system geometry.

When using the thermal circuit presented in Fig. 4 to analyze heat transfer in macro and microfluidic systems, we implicitly assume that the thermophysical properties of the confined fluid, the nature of the water flow, and the magnitude of the Kapitza resistance are all independent of tube geometry. In nanofluidic devices, where non-continuum molecular interactions dominate system performance, both the thermophysical properties of the confined water and the mechanisms governing water flow are functions of tube diameter. However, since neither the influence of nanoscale confinement on the water thermal conductivity nor the effect of non-continuum flow mechanisms on heat transfer are understood, the relation between $R_{c,c}$ and tube diameter is yet unknown. Moreover, the nature and magnitude of R_k across the water/CNT boundary has not been quantified.

III. Molecular Dynamics Simulation

A. Introduction and Overview

The small length and time scales associated with nanoscale transport phenomena limit the ability of laboratory experiments to resolve the flow of water through CNTs and heat transfer across the water/CNT interface. Molecular dynamics simulation, which can access these scales, has emerged as an alternative tool for studying the dynamics of such systems.^{16,13,14,27,32,33} Molecular dynamics is a computer simulation technique that uses Newtons laws of motion to predict the position and momentum space trajectories of a system of classical particles. The only required inputs are an intermolecular potential, which is used to calculate potential energies and forces, and an initial atomic configuration. Molecular dynamics is a highly scalable simulation technique; simulations containing over 10^5 particles can be performed on a single CPU, while simulations containing over 10^{10} particles have been performed on multi-processer computational grids.³⁴

Molecular dynamics simulations require no *a priori* assumptions concerning the nature of mass flow or energy exchange mechanisms. That is, we do not have to assume a form for the velocity profile, provide the thermophysical properties of materials within the system, or select a Nusselt number correlation from the literature. Instead, we simply allow the particles to interact via a specified intermolecular potential function and calculate properties of interest from the resulting kinematic trajectories. When properly implemented with accurate intermolecular potential functions, MD simulation can reproduce experimentally observed transport phenomena (e.g. parabolic flow profiles in large no-slip channels³⁵), predict accepted thermophysical properties (e.g. temperature dependence of water viscosity and density¹⁷), and generate additional insight into heat and mass transfer mechanisms (e.g. effect of surface wettability on liquid self-diffusion²⁵).

B. Intermolecular Potential Functions

When simulating a water/CNT system, as depicted in Fig. 5, the carbon atoms and water molecules are treated as rigid objects interacting via three classical potential functions: ϕ_{ww} , which describes interactions between water molecules, ϕ_{cc} , which describes interactions between carbon atoms, and ϕ_{cw} , which describes interactions between carbon atoms and water molecules. The form of each potential function is parameterized to approximate the true quantum mechanical interactions (e.g. electron dispersion, orbital overlap, electron exchange, etc.) observed experimentally or calculated numerically from electronic structure

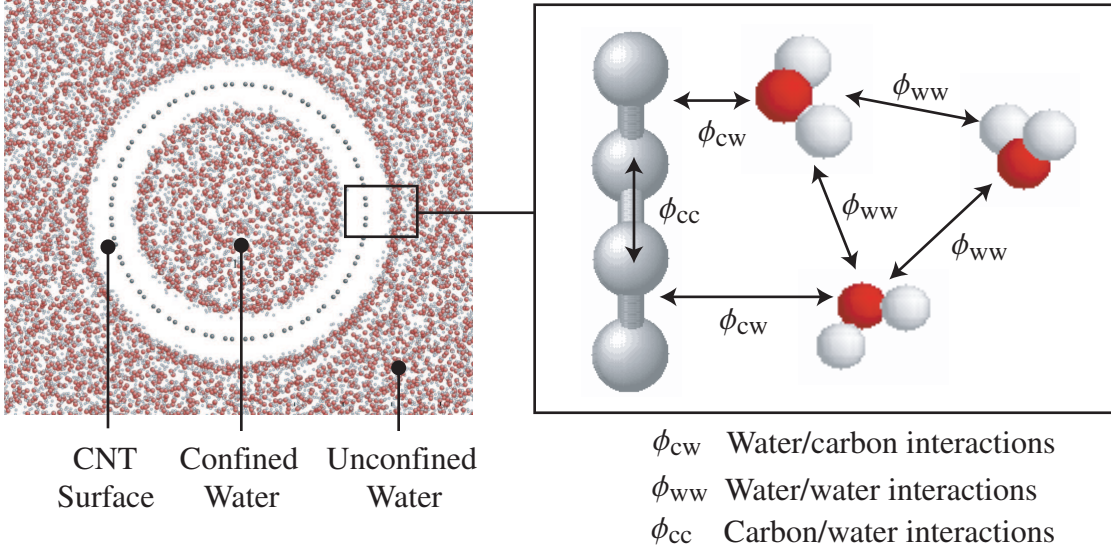


Figure 5: Cartoon depicting carbon/carbon and water/water and carbon/water interactions in an MD simulation

calculations. The intermolecular potential is the most important simulation input and has the greatest influence on the accuracy of the simulation predictions.

Water molecule interactions can be modeled using the TIP5P potential,¹⁷ where each water molecule consists of one electrostatically-neutral oxygen atom, two positively-charged hydrogen atoms, and two negatively-charged but massless interaction sites. The relative positions of the oxygen and hydrogen atoms correspond to known molecular structure data, while the positions of the charged interaction sites were tuned to reproduce experimentally-observed properties of bulk water.¹⁷ The three atoms and two interaction sites are fixed with respect to a local basis set and each molecule has zero net-charge. The interaction between two water molecules, a and b , is a combination of one Lennard-Jones (LJ) interaction between the oxygen atoms, and sixteen electrostatic interactions between the two hydrogen atoms and two charge sites on each molecule:

$$\phi_{ww} = 4\epsilon_{OO} \left[\left(\frac{\sigma_{OO}}{r_{OO}} \right)^{12} - \left(\frac{\sigma_{OO}}{r_{OO}} \right)^6 \right] + \sum_{i=1}^4 \sum_{j=1}^4 \frac{1}{4\pi\epsilon_o r_{ij}} q_i q_j. \quad (15)$$

In Eq. (15), ϵ_{OO} and σ_{OO} are the LJ parameters for the oxygen-oxygen interaction, r_{OO} is the oxygen-oxygen separation distance, q_i is the charge on site i of molecule a , q_j is the charge on site j of molecule b , ϵ_o is the permittivity of free space, and r_{ij} is the charge site separation distance. The potential parameters and charges are specified by the potential developers.¹⁷

Among water models suitable for large-scale (>1000 water molecules) MD simulation, the TIP5P potential most accurately reproduces the thermophysical properties and molecu-

lar behavior of water. For example, the average error (with respect to accepted experimental measurement) in the density from 235.5 K to 335.5 K at 1 atm is 0.006 kg/m³. The TIP5P-predicted self-diffusion coefficient and latent heat of vaporization at 298 K and 1 atm are within 10% and 1% of the experimental values. Moreover, the molecular radial distribution function predicted using TIP5P is nearly indistinguishable from that measured during Rayleigh light scattering experiments.¹⁷ Owing to its accurate predictive capabilities, the TIP5P model has been applied to a wide range of biological,³⁶ chemical,³⁷ and engineering systems.³⁸

Interactions between carbon atoms within a CNT can be modeled using a modified Morse potential:

$$\phi_{cc} = K_r (e^{(-\gamma|r_{ij}-r_c|)} - 1)^2 + \frac{1}{2}K_\theta (\cos \theta_{ijk} - \cos \theta_c)^2 + \frac{1}{2}K_\phi (1 - \cos 2\phi_{ijkl}), \quad (16)$$

where r_{ij} is the separation between bonded atoms i and j , $\cos \theta_{ijk}$ is the angle formed by atoms i , j , and k (see Fig. 12), and ϕ_{ijkl} is the torsional angle between atoms i , j , k , and l . The constants K_r , K_θ , and K_ϕ are the stretch, bend, and torsional force coefficients, while r_c and θ_c are the reference geometry parameters for graphene. The stretch and bending parameters, as originally proposed by Quo *et al.*,³⁹ describe the geometry of graphite and reproduce its phonon properties. The torsional parameter, which is needed to reproduce the strain due to CNT curvature, was evaluated by Walther *et al.* using electronic structure calculations.⁴⁰

The most widely used water molecule/carbon atom interaction potential, which is currently implemented in our MD code, is a LJ potential given by:

$$\phi_{cw} = 4\epsilon_{CO} \left[\left(\frac{\sigma_{CO}}{r_{CO}} \right)^{12} - \left(\frac{\sigma_{CO}}{r_{CO}} \right)^6 \right], \quad (17)$$

where r_{CO} is the carbon atom/oxygen atom separation distance, ϵ_{CO} is the depth of the energy well, and σ_{CO} is the length scale. This potential has been used to model the behavior of water molecules near CNTs with diameters ranging from 0.8 nm to 10 nm and water molecules near flat graphene sheets.^{25,41}

The LJ potential is a model of atomic repulsion due to overlapping electron orbitals and atomic attraction due to atomic dipole dispersion (i.e. van der Waals forces). The carbon atoms in a CNT are sp^2 hybridized, meaning that each carbon has one delocalized π -electron. Thus, in addition to carbon-oxygen LJ interactions and possible carbon-hydrogen interactions,⁴² water molecules may also interact with this delocalized electron. Moreover, the water/CNT potential presented in Eq. 17 is a two-body potential, meaning it depends on only the relative positions of the oxygen and carbon atoms. The true quantum mechanical

interactions between a water molecule and the CNT are likely to depend on both the relative orientation of the water molecule with respect to the carbon surface and the tube diameter.

We believe that the potential presented in Eq. (17) captures the dominant components of the water/CNT interaction.⁴³ We also note that this potential has been used in MD simulation to successfully predict transport behavior later observed experimentally.⁵ However, additional potential development is necessary to determine if more sophisticated intermolecular potentials, which will lead to more accurate computer predictions, are indeed necessary. Using an improved potential, our MD simulations will more accurately diagnose the flow and heat transfer characteristics in nanofluidic devices, and become a better guide to experimentalists and designers seeking to design such water/CNT systems.

C. Data Collection

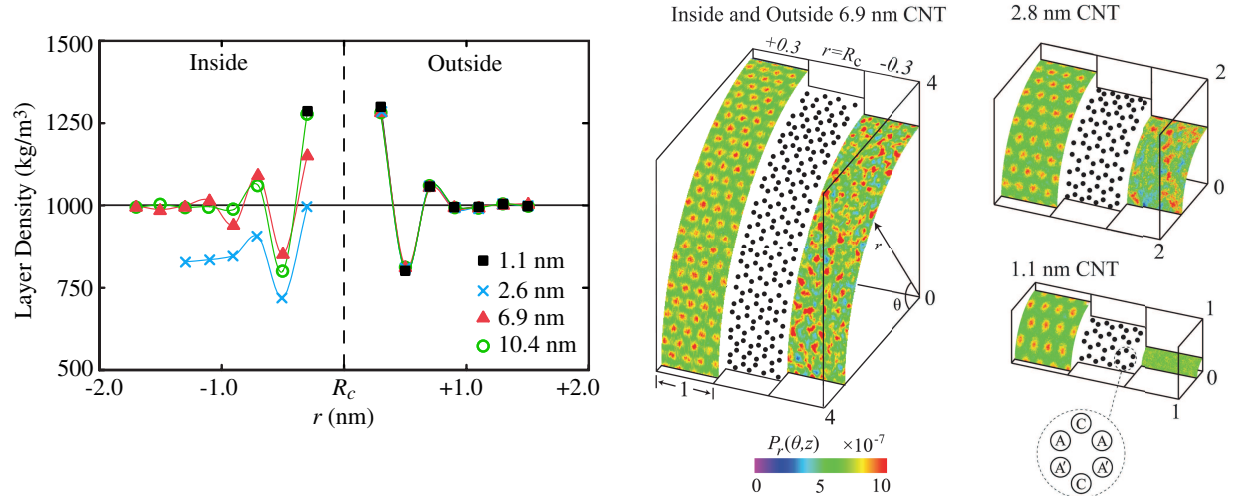
The net force (which is proportional to the spatial derivative of the potential function) on each molecule is equal to the sum of all individual interparticle interactions. When combined with the instantaneous particle kinematics, the net force is used to advance the particle position and velocity vectors over some predefined timestep δt . New interparticle forces are then evaluated using these updated positions and once again combined with the new velocity vectors. The positions are advanced once again and the process repeats. My typical water/CNT system contains 3000 water molecules, 10000 carbon atoms, and runs for 2 million 0.5 ps timesteps. This takes approximately 15 days of computer runtime. Over the next six months I plan to work with the Pittsburgh Supercomputer Center (PSC) to parallelize my MD code and reduce the computer runtime.

Using tools from statistical mechanics, the interparticle interactions and resulting kinematic trajectories can be used to predict the thermophysical properties of the water. For example, the average water temperature, $\langle T_w \rangle$, can be found from,

$$\langle T_w \rangle = \frac{\left\langle \sum_i^N K_i \right\rangle}{(6N_w - 6)k_B}, \quad (18)$$

where K_i is the kinetic energy of water molecule i , k_B is the Boltzmann constant, and N_w is the number of water molecules. The average pressure, $\langle P_V \rangle$, within a sub-volume, V_s , contained within the system can be found using a second virial expansion []:

$$\langle P_V \rangle = \left\langle \frac{N_s k_B T_s}{V_s} \right\rangle + \frac{1}{3V_s} \sum_i \sum_{j>i} \sum_{a=1}^4 \sum_{b=1}^4 \frac{r_{ab} \nabla \phi_{ab}}{r_{ab}^2} \cdot (\mathbf{r}_{ai} \cdot \mathbf{r}_{bj}) \quad (19)$$



(a) Water density inside and outside CNTs of different diameter. The symbol R_c indicates position of the CNT radius and r indicates radial displacement from the CNT surface

(b) Water molecule distribution near the CNT surface. Warmer shades indicate higher water molecule position probabilities, $P_r(\theta, z)$. Note that the distribution of the confined water molecules becomes more uniform with decreasing tube diameter.

Figure 6: Results from previous MD simulation of water/CNT systems.

where N_s is the number of particles in V_s and T_s is the average temperature of the molecules inside V_s . The symbol \mathbf{r} defines the particle position and the i and j indices denote molecules inside the sub-volume. Many other properties (e.g. density, chemical potential, coordination number, etc.) can be predicted. For example, as shown in Fig. 6 we previously used MD simulation to predict the radial density of water molecules inside a CNT and the molecular distribution near the carbon surface.³⁸ Note that outside the CNT, the water density profile and molecular distribution is invariant with tube diameter. Inside the tube, however, both the density profile and the distribution of water molecules near the carbon surface are functions of CNT diameter.

Note that for computational efficiency, the carbon atoms within these previous simulations were fixed in space (e.g. the CNT is “frozen”). In an extension of our previously reported work on monatomic LJ solid-fluid interfaces,²⁵ we found that fixing the solid atoms had no detectable effect on the density, distribution, and diffusion characteristics of the interfacial liquid. Others have reported that fixing the carbon atoms has little effect on the dynamics of adjacent water.¹⁹ When investigating heat transfer to the confined fluid, however, we will allow the carbon atoms to move and interact with each other.

In addition to calculating thermophysical properties, we can also use MD simulation and tools from statistical mechanics to predict the transport coefficients of the water/CNT system. Transport coefficients, such as the thermal conductivity, viscosity, and diffusion coefficient, describe the response of a system to an imposed macroscopic gradient. By understanding the molecular mechanisms that govern the transport coefficients and how these mechanisms are affected by confinement, we can elucidate the physics responsible for the enhanced flow (and potentially ultra-low heat transfer) in water/CNT systems.

Both equilibrium and non-equilibrium techniques can be used to predict transport coefficients and investigate transport phenomena. In an equilibrium MD simulation, transport coefficients are predicted by applying linear response theory to systems with a constant number of particles, constant system volume and constant system energy (the *NVE* ensemble). Linear response theory requires that we evaluate the infinite time integral of a time correlation function. For example, the thermal conductivity, k , of a material can be found from the relation:

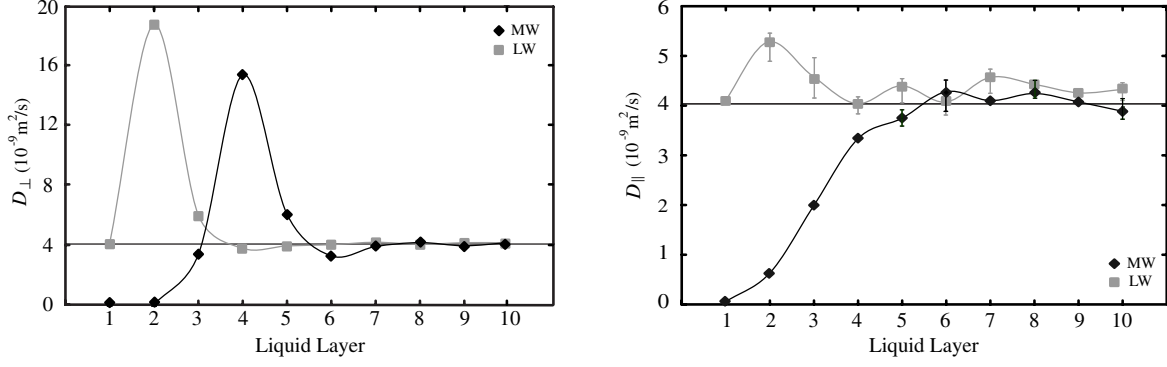
$$k = \frac{1}{3Vk_B T^2} \int_0^\infty \langle \mathbf{S}(0) \cdot \mathbf{S}(t) \rangle dt, \quad (20)$$

where \mathbf{S} is the heat current vector (which describes the instantaneous net heat flux within the system) and the angled brackets denote an autocorrelation.¹³ Since the autocorrelation function decays to zero, we can numerically approximate integration over the infinite time integral with good accuracy. The viscosity of a fluid, μ , can also be predicted from equilibrium simulation using time correlation functions:

$$\mu = \frac{1}{k_B TV} \int_0^\infty \frac{1}{9} \sum_{a=1}^3 \sum_{b=1}^3 \langle \mathbf{J}^{aa}(0) \cdot \mathbf{J}^{bb}(t) \rangle dt, \quad (21)$$

where \mathbf{J} is the momentum current vector (which describes the instantaneous location of the momentum center of mass).¹³

In a previous investigation, we used equilibrium MD simulation to predict the effect of surface wettability on liquid argon self-diffusion near a planar solid surface.²⁵ As presented in Fig. 7, we found that the components of the liquid self-diffusion coefficient tensor were functions of both surface wettability and distance from the solid. This result suggests that the mass transport behavior of liquid atoms within a solid channel can be passively tuned by controlling the surface wettability. A large variety of other linear response formulations, describing the self-diffusion coefficient, slip length, the friction constant on a diffusing particle, nuclear magnetic resonance, etc., are available in the literature.⁴⁴ Because these correlation methods utilize the naturally evolving molecular trajectories, they give a clear picture of the molecular interactions and mechanisms governing the transport coefficient.



(a) Perpendicular-to-surface self-diffusion coefficient of liquid argon near a planar solid surface

(b) Parallel-to-surface self-diffusion coefficient of liquid argon near a planar solid surface

Figure 7: Components of liquid argon self-diffusion coefficient tensor near a more-wetting (MW) and less-wetting (LW) planar solid. The solid horizontal line indicated the bulk liquid value and each liquid layer is approximately 0.3 nm thick.

In non-equilibrium MD simulation, the transport coefficients are measured directly by predicting the response of a system to an externally applied forcing function (e.g. an applied pressure gradient to induce flow or an applied heat flux to establish a temperature gradient). This procedure is similar to experiment at the macroscale, where transport coefficients are determined by comparing the flux of conserved quantities to the gradient of the corresponding affinities. Unlike equilibrium time-correlation functions, where the signal to noise ratio may be small, non-equilibrium simulation allows us to apply a much larger signal and more clearly predict the response of the system. Non-equilibrium simulation also allows us to investigate other system parameters, such as system thermal resistances and flow velocity profiles. However, unlike linear response theory, the non-equilibrium technique provides little insight into the molecular interactions and molecular mechanisms contributing to the transport coefficient.

In the proposed research, as discussed more fully in Sec. IV, I will use both equilibrium and non-equilibrium simulation techniques to accurately predict the magnitude of the transport coefficients and clearly identify the underlying molecular mechanisms. Our research group has worked extensively with both Eq. (20) and non-equilibrium MD simulation techniques to relate the thermal conductivity and atomic structure of a variety of solids.

IV. Proposed Research and Preliminary Findings

A. Identify the Mechanisms Responsible for Enhanced Water Flow in CNTs

Although experimentalists have observed that water flow through CNTs is enhanced above the predictions of the no-slip Hagen-Poiseuille model, the CNT diameter range over which these flow enhancements are present and the physical mechanisms responsible for the enhanced flow are still unidentified. In this section, I discuss how I will determine range of CNT diameters over which the flow is enhanced, how I will identify the mechanisms responsible for the enhanced flow, present my preliminary research findings, and introduce my future research methodology.

I have begun my investigation using non-equilibrium MD simulation to generate a pressure gradient and induce water flow through CNTs with a range of diameters. As depicted in Fig. 8(a), the pressure gradient and flow field are established by placing a reflecting particle membrane (RPM)³⁵ at the tube entrance. The RPM operates as follows: molecules crossing the membrane in the desired flow direction pass freely; molecules crossing the membrane in the opposite direction have some probability, p , of being elastically reflected back towards the direction of flow. The magnitude of the pressure gradient inside the tube, which is tuned via the magnitude of p , is not known *a priori*. However, as demonstrated in Fig. 8(b), I can calculate this value by evaluating the pressure within several sub-volumes [using Eq. (19)] along the tube axis and performing a linear regression analysis on the resulting pressure versus position data. The volumetric flow rate and average flow velocity can be calculated precisely during the simulation. As presented in Fig. 9(a), this procedure allows me to explore the effect of pressure gradient on water flow over a range of pressure gradients and tube diameters.

Typical pressure gradients applied to actual water/CNT membrane systems are on the order of 10^{11} Pa/m. The flow velocities generated by such a pressure gradient range from 0.01 m/s to 0.1 m/s. In MD simulation, thermal background noise during the simulation makes resolving such small flow velocities nearly impossible. The smallest flow velocities we can confidently resolve are between 1 m/s and 10 m/s, and the smallest detectable pressure gradients are between 10^{13} Pa/m and 10^{14} Pa/m. My preliminarily findings [see Fig. 9(a)] show that the average volumetric flow rate of water inside the CNTs, $\overline{Q_d}$, is linearly proportional to the applied pressure gradient:

$$\overline{Q_d} = \gamma_d \frac{\partial P}{\partial z}, \quad (22)$$

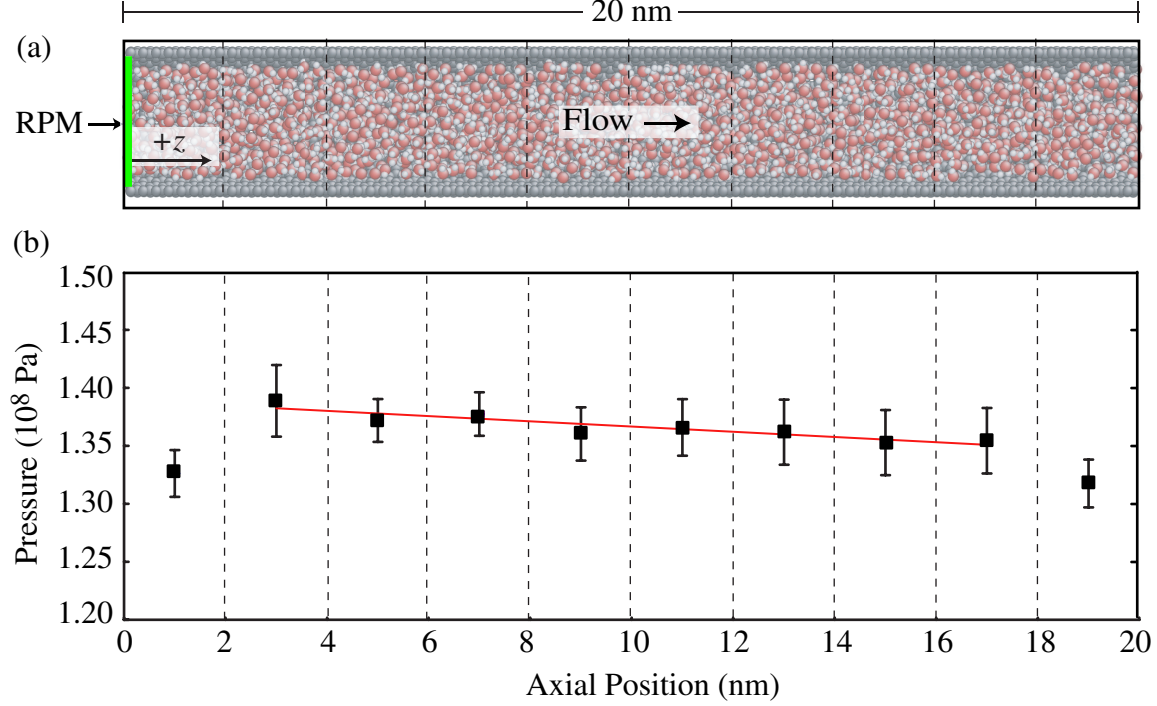


Figure 8: Water flow through a 2.8 nm diameter CNT. In this trial, the magnitude of the pressure gradient was 2.3×10^{14} Pa/m, the average flow velocity was 7.5 m/s and, and volumetric flow rate was 7.7×10^{-17} m³/s. The mechanical susceptibility, as predicted from this trial, is then 2.0×10^{-31} m⁵.s/kg

where γ_d is a proportionally constant we call the diameter-specific mechanical susceptibility. Thus, even though we must simulate higher velocities and larger pressure gradients than experimentalists, our results and data should be readily comparable to laboratory results.

The linear relation presented in Eq. (22) is consistent with Eq. (5), where γ_d for the slip-modified Hagen-Poiseuille model is a combination of the water viscosity, slip length, and tube diameter:

$$\gamma_d = \frac{\pi [(d/2)^4 + (d/2)^3 L_s]}{8\mu}. \quad (23)$$

Note that γ_d is inversely proportional to viscosity, but linear related to the slip length. Thus, when the liquid viscosity is high, γ_d is low; when L_s is long, γ_d is large. Of course, Eq. (23) is inapplicable to water/CNT systems where the Hagen-Poiseuille model breaks down. However, even within such nanofluidic systems, γ_d is likely to be inversely related to the viscosity of the water and directly related to the strength of the water-carbon interaction force. I therefore suspect that the key to identifying the mechanisms responsible for the enhanced flow is identifying the dependence of the water viscosity and the nature of the water-carbon interactions (which is the non-continuum analogy of slip length) on tube

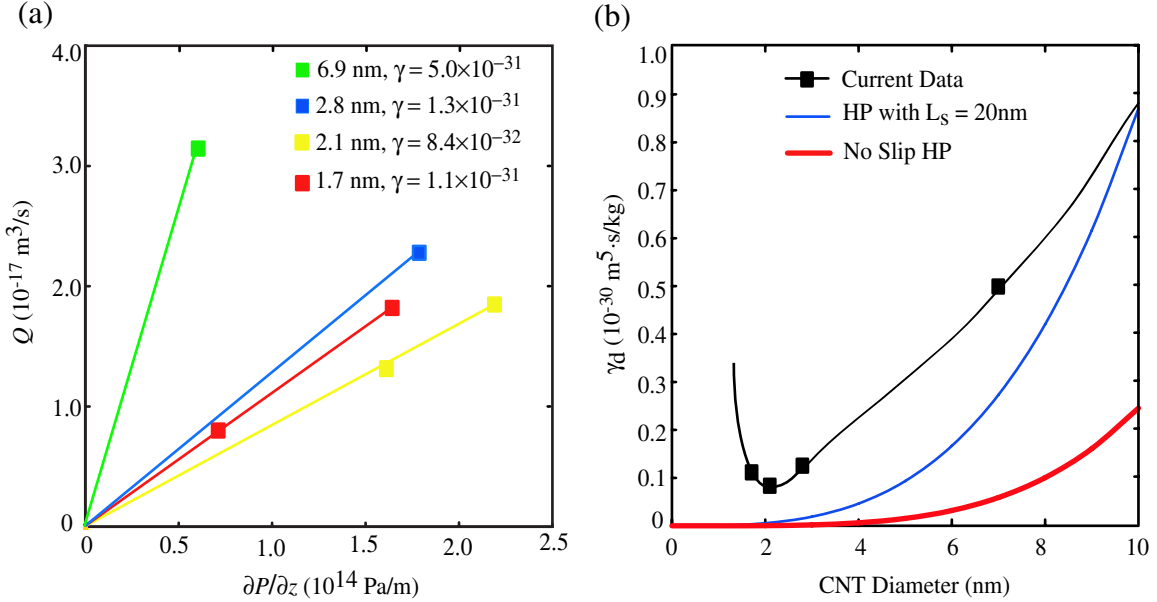


Figure 9: (a) Volumetric flow rate in various CNTs versus applied pressure gradient. The units of γ are $\text{m}^5 \cdot \text{s/kg}$ (b) Plot of γ versus tube diameter. Also shown is the Hagen-Poiseuille (HP) predicted γ for a no-slip system and system where $L_s = 20 \text{ nm}$. The solid line through the current data is to guide the eye.

diameter.

We previously reported that water confined inside tubes with diameters smaller than 3 nm does not recover bulk-like water properties.³⁸ We also qualitatively demonstrated that inside such small CNTs, interactions between water molecules and the carbon surface are too weak to influence the molecular distribution and orientation within the interface region [see Fig. 6(b)]. In CNTs with diameters between 3 nm and 10 nm, we found that the confined water does recover bulk-like water properties, but, compared to the smaller tubes, the distribution and orientation of the water molecules near the CNT surface is closely related to the atomic structure of the carbon surface (suggesting that interactions between the water and the carbon surface became more prevalent in these larger tubes). In CNTs with diameters greater than 10 nm, we found that further increasing the tube diameter had no additional effect on either molecular behavior across the interfacial region or thermophysical properties of the confined fluid.³⁸

Based on these findings, I predict that the water confined inside the sub-3 nm CNTs has a reduced absolute viscosity (due to the reduced liquid density and breakdown of the hydrogen bonding network), thereby increasing the diameter-specific mechanical susceptibility coefficients and enhancing water flow through the CNTs. I believe this enhancement to γ_d

is further amplified by the limited influence of the water/CNT interactions on water within such tubes. As the tube diameter increases from 3 nm to 10 nm, I expect the viscosity of the confined water to increase and approach the bulk water value. Although γ_d for such tubes will still be greater than that predicted using bulk values and Eq. (23), this increase in viscosity, coupled with the increasing influence of the water/carbon interactions, will cause γ_d to approach the continuum limit. Finally, inside CNTs with diameters greater than 10 nm, where additional increases in tube diameter have no effect on the thermophysical behavior of the confined fluid, I expect fluid flow to be governed by the slip-modified Hagen-Poiseuille relation. Within these larger tubes, I expect the slip length (which we can predict using equilibrium techniques or calculate directly from the radial velocity profile) to be invariant with tube diameter and the viscosity to be equal to the bulk water value.

To test this hypothesis, I will continue working with the pressure-driven flow system and explore the effects of tube diameter on γ_d . This first step is important; the flow rate versus pressure data will help me identify the range of CNT diameters over which the flow enhancement is present, and allow me to predict the degree of flow enhancement for other tubes. Even without additional insights into the mechanisms responsible for the enhanced flow, this mechanical susceptibility data will be useful to experimentalists and engineers seeking to design nanofluidic devices with tailored mass transport properties.

After using the pressure-driven flow system to identify the range of CNT diameters over which the flow is enhanced, I will use equilibrium simulation and Eq. (21) to examine the influence of tube diameter on confined water viscosity. This work will allow me to test my preliminary hypothesis that water viscosity increases with tube diameter, and conclude if changes to the water viscosity are indeed a mechanism responsible for the enhanced flow. The viscosity of water inside CNTs has not yet been explored, and the spatially density profiles (and other non-continuum effects) will make predicting the viscosity difficult.

Finally, I will examine the effect of CNT diameter on water/carbon surface interaction strength. Although we qualitatively explored this trend in our previous report, I will move beyond these results by explicitly quantifying the interaction strength using the linear response methods of Barrat and Chiaruttini.¹⁰ This measurement will test my earlier hypothesis that weak water/CNT interactions lead to enhanced flow rates, and allow me to identify the range of CNT diameters over which the water/CNT interactions contribute to the enhanced flow.

B. Examine Heat Transfer to the Confined Fluid

Both computer simulation and laboratory experiment have demonstrated that heat transfer through the unconfined liquid/CNT interfacial region is impeded by a very large Kapitza resistance.^{11,12} Although not yet measured, a similar Kapitza resistance is likely present between the confined water and the CNT surface as well. Moreover, the effects of high mass transport on convective heat transfer in nanofluidic devices, as foreshadowed by slip-based corrections to the Nusselt number, suggest that heat transfer to water flowing inside CNTs is further reduced by large convective thermal resistances. These high Kapitza and convective thermal resistances may insulate the flowing fluid from the surrounding environment, allowing for the development of exciting thermally isolated, high flow rate engineering systems. In this section I discuss how I will use MD simulation to examine Kapitza resistance across the water/CNT boundary and how I will study convective heat transfer from the CNT to the confined fluid.

I will begin my investigation by using non-equilibrium MD simulations to generate a radial heat flux and radial temperature profile through quiescent confined and unconfined water. Using the methods illustrated in Fig. 10(a), I will maintain the temperature of the liquid core at 290 K and the temperature of the liquid far-field at 320 K. Heat will flow from the high-temperature far-field region, through the unconfined water, across the CNT surface, and into the low temperature liquid core. This process will generate a temperature profile across the confined and unconfined fluids, as depicted graphically in Fig. 10(b). I can readily predict the heat flux through the system by measuring the temperature profile across the unconfined water. Knowing the temperature drop at the confined/CNT and unconfined water/CNT boundaries, I can evaluate both Kapitza resistances using Eq. (13).

To elucidate the effect of surface curvature on Kapitza resistance, I will apply this non-equilibrium simulation procedure to 10, 6.9, 4.9, 2.6 and 1.1 nm diameter CNTs [armchair CNTs with chirality vectors of (75,75), (50,50), (35,35), (20,20), and (8,8)]. We previously reported that surface curvature has no effect on water molecule density or distribution outside the CNT. Based on these results, I expect the Kapitza resistance of the unconfined water/CNT boundary to be invariant with tube diameter. Inside tubes with diameters greater than 10 nm, where increasing the CNT diameter has no detectable effect on molecular behavior, I expect the Kapitza resistance of the confined water/CNT boundary to be equivalent to the Kapitza resistance of the unconfined water/CNT boundary. Within sub-10 nm CNT, I expect the Kapitza resistance to increase with decreasing CNT diameter. This hypothesis is consistent with our previous finding that the coupling between confined water molecules and the carbon surface decreases with tube diameter [see Fig. 6(b)].

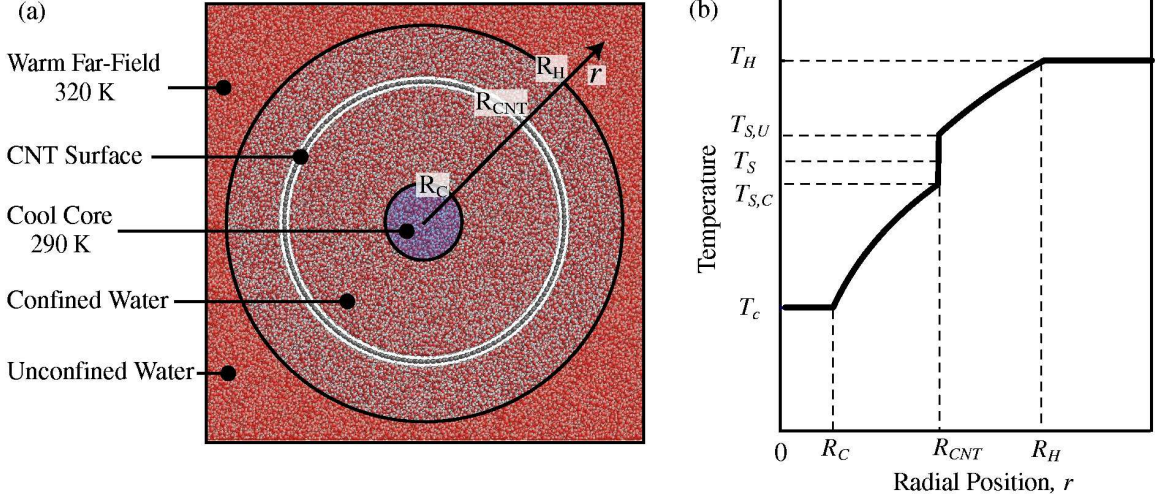


Figure 10: Non-equilibrium MD technique and resulting temperature gradient used to predict the Kapitza resistance.

Having predicted the Kapitza resistance across the solid-liquid interface and examined its dependence on tube diameter, I will set the confined fluid in motion (using the techniques described in Sec. A) and predict the resistance to convective heat transfer. The unconfined fluid will remain quiescent. As depicted schematically in Fig. 11, I will use a non-equilibrium simulation technique similar to that used to predict the Kapitza resistances. However, instead of cooling the water molecules in the liquid core, I will cool the water entering the CNT to 290 K while maintaining far-field temperature at 320 K. Heat will flow from the warm far-field region to the confined region, thereby raising the temperature of the flowing fluid. I will be able to calculate the temperature of the fluid exiting the tube during the simulation, and predict the steady state heat flux through the system from the radial temperature profile across the unconfined fluid.

The heat flux from the confined fluid to the unconfined fluid is given by:

$$q'' = \frac{T_f - \bar{T}_m}{\bar{R}_{c,c} + R_{c,k} + R_{u,k} + R_{u,c}}, \quad (24)$$

where \bar{T}_m is the mean temperature of the confined fluid, which is found from the axial temperature profile, and \bar{R}_c is the average confined convective resistance. Having already predicted the Kapitza resistances, the conductive thermal resistance of the unconfined water, and the steady state heat flux through the system, I can explicitly solve Eq. 24 for \bar{R}_c :

$$\bar{R}_c = \frac{T_f - \bar{T}_m}{q''} - R_{c,k} - R_{u,k} - R_{u,c}. \quad (25)$$

Just as with the Kapitza resistance, I will apply this non-equilibrium simulation procedure

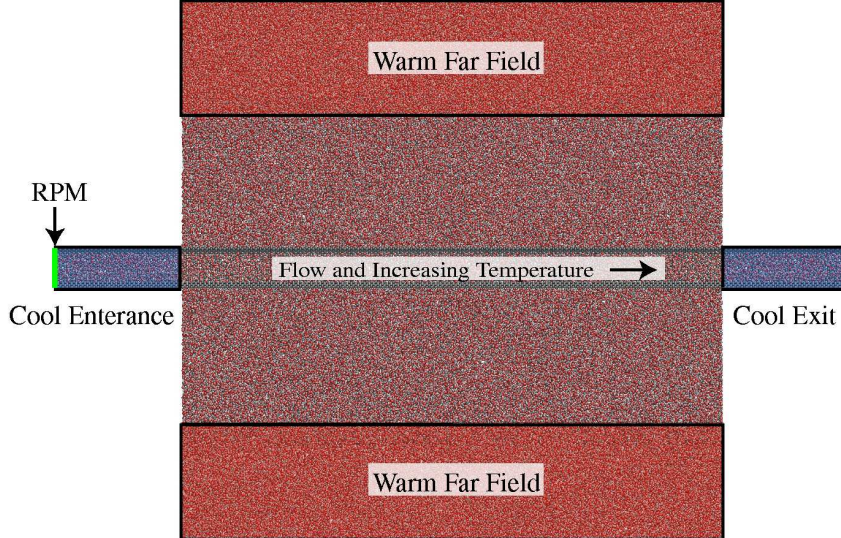


Figure 11: Non-equilibrium MD technique used to determine convective heat transfer resistance inside the tube.

to 10, 6.9, 4.9, 2.6 and 1.1 nm diameter CNTs to determine the effect of tube diameter on \bar{R}_c . By quantifying these thermal resistances, I can determine if water confined within CNTs is indeed insulated from the surrounding environment. Moreover, by examining the dependence of the Kapitza and convective thermal resistances on tube diameter, I can determine how this thermal isolation varies with tube diameter and water mass flow rate. As with the mechanical susceptibility and Kapitza resistance, I expect the convective resistance in sub-3 nm diameter CNT to increase with decreasing tube diameter. In tubes with diameters larger than 10 nm, however, I expect \bar{R}_c to be directly proportional to the CNT diameter (as observed at the micro and macroscales).

C. Improve the Water/CNT Intermolecular Potential

A thorough understanding of the water/CNT interaction potential is necessary to predict the flow behavior of water confined within CNTs and heat transfer characteristics at the water/carbon interface. As a preliminary step, many have worked to calculate the interaction energy between water and a flat graphene sheet (which can be viewed as a CNT of infinite diameter).^{19,45-49} The resulting interaction energies and intermolecular potential functions have been used in water/CNT systems. However, a focused investigation into the water/CNT binding energy and the associated potential energy function has yet to be performed by either theorists or experimentalists. The purposes of this section are to introduce the techniques I (along with collaborators at the University of Pittsburgh) will use to evaluate the water/CNT

potential function and discuss the anticipated form of the intermolecular potential.

Outside of direct measurement (which is difficult due to the small CNT geometry), *ab initio* electronic structure calculations are the most promising method for predicting the water/CNT interaction energy. As the name suggests, *ab initio* calculations are “from the beginning” and are performed by approximating solutions to the time-independent Schrödinger equation. The only parameters necessary to perform an electronic structure calculation are an atomic configuration, an appropriate electron basis set, and an appropriate level of theory.⁵⁰

At the heart of electronic structure calculations is the electron basis set. An electron basis set is the mathematical description of the electron orbitals within a system and is typically the constituent atomic orbitals (e.g. $1s$, $2s$, $2p$, etc.).⁵¹ The molecular orbitals, which describe the electronic structure of the system, are then formed from a linear combination of these atomic electron orbitals (i.e. each atomic orbital is given an appropriate weighting coefficient). In this work, as in previous investigations of water/graphite interactions,⁴⁹ we will utilize the aug-cc-pVDZ basis set. This basis set assigns three s -orbitals and two p -orbitals to each hydrogen atom, and four s -orbitals, three p -orbitals, and two d -orbitals to each carbon and oxygen atom. Consistent with previous work,^{48,49} we utilize a Møller-Plesset second-order perturbation (MP2) level of theory. The MP2 level is a computationally inexpensive way of including most of the electron correlation effect into baseline Hartree-Fock calculations.

Using electronic structure calculations to investigate interactions within and between graphite sheets, Ruuska and Pakkanen demonstrated that inter-sheet interactions do not influence the average atomic charge or density of orbital energy states on either sheet.⁵² Moreover, Feller and Jordan demonstrated that the binding energy between water and a $C_{54}H_{18}$ fragment is almost identical to the binding energy between water and a $C_{96}H_{24}$ fragment.⁴⁹ They also report good agreement (binding energies within 10%) between the $C_{96}H_{24}$ fragment and an even smaller $C_{24}H_{12}$ fragment. Thus, instead of calculating the binding energy between a water molecule and the entire CNT, we need only calculate the interaction energy between water molecules and a small, single-layer carbon fragment. Since this work represents a first-order analysis of a previously uninvestigated system, we initially use the $C_{24}H_{12}$ structure fragment depicted in Fig. 12. Although using a larger carbon fragment would provide slightly more accurate predictions of the water/CNT binding energy, single point energy calculations with the smaller fragment (which take about 12 hours of computer runtime) are approximately 25 times faster than those with larger fragments.

To properly calculate the water/CNT electronic structure, we will work with Dr. Kenneth Jordan of the University of Pittsburgh and Glen Jenness, a Ph.D. candidate in the

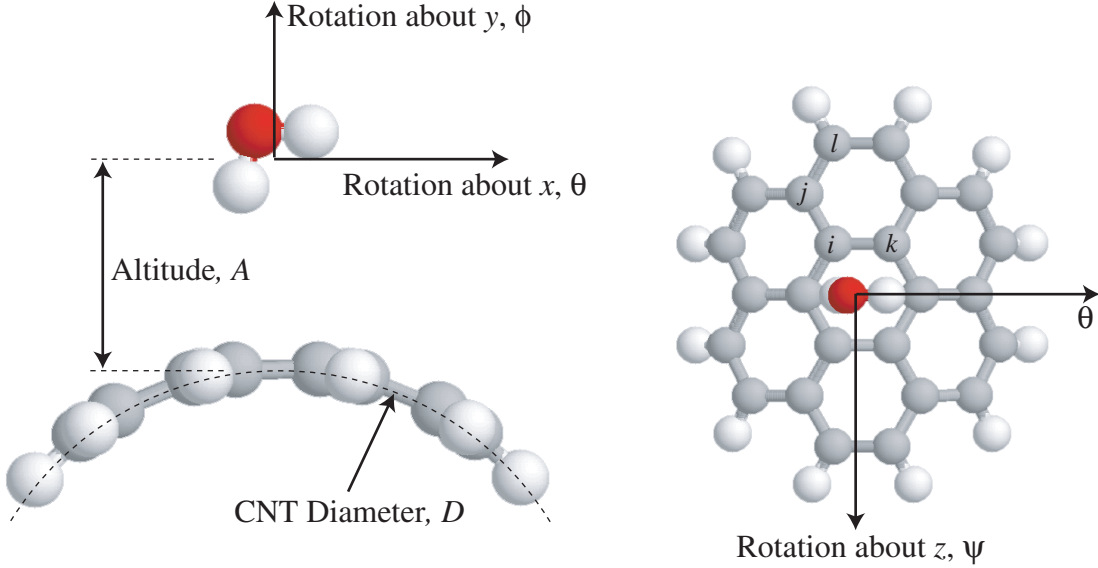


Figure 12: Water molecule above curved $C_{24}H_{12}$ carbon fragment. The altitude of the water molecule is 0.42 nm and the CNT diameter is 1.1 nm. Note that due to the symmetry of the system, we need only scan ϕ from 0 to $\pi/2$.

Jordan group. They have access to efficient codes for performing such electronic structure calculations and extensive computational resources. We are currently working together to set-up and run the electronic structure codes on their parallel computing network. My responsibilities during this set-up process include generating water/CNT structures for use in their code and working with Glen to identify the components of the water/CNT binding energy. After data collection is complete, I will convert the quantum mechanical-based intermolecular potential energy data into a classical intermolecular function for use in MD simulation.

As presented in Fig. 12, the water/CNT interaction energy is a function of five independent variables: rotation about the x -, y -, and z -axes, molecular altitude, and the CNT diameter. Depending on the slope of the potential energy landscape, the increments of the angular scans will be between 5 and 10 degrees and the increments of the altitude scans will be between 0.1 and 0.3 nm. We will also examine water molecules confined inside the CNT (i.e. interacting with the concave side of the tube).

We will begin by examining the effect of water molecule orientation and water molecule altitude on binding energy near a flat $C_{24}H_{12}$ carbon fragment. Comparing these findings to previously reported water/graphene results will validate our system set-up and calculation procedure. Moreover, these predictions will serve as a benchmark for identifying both the range of CNT diameters over which surface curvature is relevant and how surface curvature

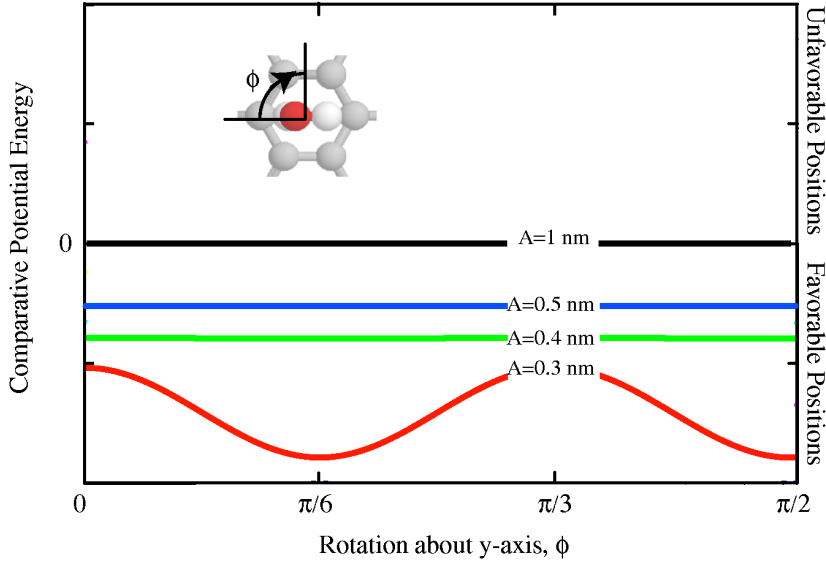


Figure 13: Anticipated effect of water molecule orientation on water/CNT potential energy at various altitudes.

influences the nature of the water/CNT interaction energy. We will then investigate the effect of water molecular orientation and molecular altitude on binding energy near curved carbon fragments corresponding to 10, 6.9, 4.9, 2.6 and 1.1 nm diameter CNTs. Additional diameters will be investigated if higher-resolution data is needed to discern the effects of CNT diameter on potential energy.

Our preliminary findings [see Fig. 6(a)] indicate that the minimum water molecule altitude for all CNTs is approximately 0.3 nm. At this altitude, as depicted in Fig. 13, I expect strong interactions between the oxygen atoms and the inner-most carbon atoms to generate energetically more-favorable and energetically less-favorable regions near the CNT surface that vary with molecular orientation. As the molecular altitude is increased from 0.3 to 0.4 nm, interactions with these inner-most carbon atoms will become less distinct, the difference in energy between the favorable and unfavorable regions will become smaller, and the altitude-average binding energy will become less negative. As the altitude is increased beyond 0.4 nm, I expect the binding energy to become invariant with molecular orientation and the water/CNT binding energy to monotonically increase to zero. Due to their low atomic number and single electron, I do not expect the hydrogen atoms to contribute significantly to the total water/CNT interaction energy.

Once we have a complete description of the water/carbon interaction energy as a function of molecular orientation, molecular altitude, and CNT diameter, we will fit the data to a continuous and differentiable function. Since dispersion interactions [modeled using the LJ

potential presented in Eqn. (17)] are responsible for most of the water/CNT interactions, I expect the orientation-modified water/CNT potential to be of the form:

$$\phi_{cw} = B(r) \cos\left(\frac{\phi}{a(r)}\right) \left[\left(\frac{\sigma_{CO}}{r}\right)^{12} - \left(\frac{\sigma_{CO}}{r}\right)^6 \right], \quad (26)$$

where r is the shortest distance between the oxygen atom and the carbon surface, and $B(r)$ and $a(r)$ are diameter-specific functions and constants describing the orientation-dependant behavior and gradual decay of the energetically favorable and energetically unfavorable regions near the CNT surface.

We will implement this new water/CNT potential function into our MD code and examine its effect on the predicted flow rates and heat transfer. With this new potential, our MD simulations should better reproduce the experimentally observed high mass flow rates and better predict the effects of confinement on the thermophysical properties of water. This means we can more explicitly determine the molecular interactions responsible for the enhanced flow, more accurately quantify heat transfer to the confined fluid, and more precisely guide experimentalists seeking to construct more complicated flow systems and networks. Furthermore, the potential will be useful to others using MD or Monte Carlo simulation techniques to investigate different water/CNT transport or interaction phenomena.

V. Outcomes and Schedule

The outcomes of the proposed research will be:

1. The development a water/CNT interaction potential for use in computer simulation that includes the effects of surface curvature and molecular orientation.
2. The identification of the range of CNT diameters over which the volumetric flow rates are enhanced and precise quantification of this enhancement.
3. The quantification of how confinement influences both water viscosity and interactions with the CNT surface.
4. A prediction of the Kapitza resistance across the water/CNT boundary and an determination of its dependance on tube diameter.
5. A prediction of the convective thermal resistance inside CNTs, and determination if heat transfer to confined water can be passively tuned by tailoring the dimensions of the water/CNT system.

My research timeline is summarized in Fig. 14. In Tasks 1, 2, and 3, the solid bars indicated code development, testing and data collection. The open bars indicate data interpretation/dissemination.



Figure 14: Anticipated research timeline

VI. Biographical Sketch

John Alexander Thomas was born and raised in St. Paul, Minnesota. He graduated from Penn State University in December 2005 and enrolled at Carnegie Mellon University in January 2006. He was awarded a National Science Foundation Graduate Research Fellowship in 2007 and is currently a teaching assistant for undergraduate fluid mechanics.

Coursework at Carnegie Mellon

Quantum Physics, Spring 2006

Microfluidics, Spring 2006

Molecular Simulation of Materials, Spring 2006

Advanced Thermodynamics, Fall 2006

Advanced Heat Transfer, Fall 2006

Statistical Thermodynamics, Spring 2007

Small Scale Heat Transfer, Spring 2007

Advanced Mathematical Methods for Chemical Engineers, Fall 2007

Advanced Topics in Quantum Chemistry, Fall 2007

Advanced Fluid Mechanics, Anticipated Fall 2008

Peer-reviewed Journal Publications

1. J. A. Thomas and A. J. H. McGaughey, "Effect of surface wettability on liquid density, structure, and diffusion near a solid surface," *Journal of Chemical Physics* **126** (2007) 034707. Paper selected to appear in Virtual Journal of Nanoscale Science and Technology, February 5, 2007 issue.
2. J. A. Thomas and A. J. H. McGaughey, "Density, distribution, and orientation of water molecules inside and outside carbon nanotubes," To appear in *Journal of Chemical Physics*.

Conference Presentations

1. J. A. Thomas and A. J. H. McGaughey, "Effect of surface wettability on liquid structure and mobility near a solid surface," presented at 2006 APS Division of Fluid Dynamics Annual Meeting, November 2006, Tampa Bay, FL.

2. J. A. Thomas and A. J. H. McGaughey, “Molecular dynamics simulation of water inside and outside carbon nanotubes,” presented at 2007 APS Division of Fluid Dynamics Annual Meeting, November 2007, Salt Lake City, UT.
3. J. Thomas, M. Paharia, E. Landry, G. Lee, A. McGaughey, “Atomistic water droplet simulation,” presented at 2007 APS Division of Fluid Dynamics Annual Meeting, November 2007, Salt Lake City, UT.

References

- ¹GRUNER, G., Anal Bioanal Chem **384** (2006) 322.
- ²Y. YUN, Z. DONG, V. N. S. A. B. W. R. H. H. B. H. L. C. A. B. and SCHULZ, M. J., Proceedings of the Society of Photographic Instrumentation Engineers **6528** (2007) 65280T.
- ³J. LI, C. P. and XU, J., Nature **402** (1999) 253.
- ⁴M. SHIM, N. W. S. KAM, R. J. C. Y. L. and DAI, H., Nano Letters **2** (2002) 285.
- ⁵HOLT, J. K., PARK, H. G., WANG, Y., et al., Science **312** (2006) 1034.
- ⁶MAJUMDER, M., CHOPRA, N., ANDREWS, R., and HINDS, B. J., Nature **438** (2005) 44.
- ⁷J. R. WELTY, C. E. W. and WILSON, R. E., Fundamentals of momentum, heat and mass transfer, 3rd edition, p. 476, Wiley and Sons, New York, 1984.
- ⁸H. VERWEIJ, M. C. S. and LI, J., Small **3** (2007) 1996.
- ⁹STARK, A. M., Lawrence Livermore National Laboratory News Release **NR-06-05-06** (May 18, 2006).
- ¹⁰BARRAT, J.-L. and CHIARUTTINI, F., Molecular Physics **101** (2003) 1605.
- ¹¹HUXTABLE, S. T., CAHILL, D. G., SHENOGIN, S., et al., Nature Materials **2** (2003) 731.
- ¹²SHENOGIN, S., XUE, L., OZISIK, R., KEBLINSKI, P., and CAHILL, D. G., Journal of Applied Physics **95** (2004) 8136.
- ¹³ALLEN, M. P. and TILDESLEY, D. J., *Computer Simulation of Liquids*, Calrendon Press, Oxford, 1987.
- ¹⁴E. M. KOTSALIS, J. H. WALther, P. K., International Journal of Multiphase Flow **30** (2004) 995.
- ¹⁵MCGAUGHEY, A. J. H., HUSSEIN, M. I., LANDRY, E. S., KAVIANY, M., and HULBERT, G. M., Physical Review B **74** (2006) 104304.
- ¹⁶R. S. TAYLOR, L. X. DANG, B. C. G., Journal of Physical Chemistry **1996** (100) 11720.

- ¹⁷MAHONEY, M. W. and JORGENSEN, W. L., Journal of Chemical Physics **112** (2000) 8910.
- ¹⁸MAHONEY, M. W. and JORGENSEN, W. L., Journal of Chemical Physics **114** (2001) 363.
- ¹⁹WERDER, T., WALTHER, J. H., JAFFE, R. L., HALICIOGLU, T., and KOUMOUTSAKOS, P., Journal of Physical Chemistry B **107** (2003) 1345.
- ²⁰H. DAI, E. W. WONG, C. M. L., Science **272** (1996) 523.
- ²¹L. A. HOUGH, M. F. ISLAM, B. H. A. G. Y. and HEINEY, P. A., Nano Letters **6** (2006) 313.
- ²²JOSEPH, P. and TABLELING, P., Physical Review E **71** (2005) 035303(1).
- ²³C.-H. CHOI, K. J. A. W. and BREUER, K. S., Physics of Fluids **15** (2003) 2897.
- ²⁴V. S. J. CRAIG, C. N. and WILLIAMS, D. R. M., Physical Review Letters **87** (2001) 054504(1).
- ²⁵THOMAS, J. A. and MCGAUGHEY, A. J. H., Journal of Chemical Physics **126** (2007) 034707.
- ²⁶KOGA, K. and TANAKA, H., Journal of Chemical Physics **122** (2005) 104711.
- ²⁷I. HANASAKI, A. N., The Journal of Chemical Physics **124** (2006) 144708(1).
- ²⁸SEIDER, E. N. and TATE, G. E., Industrial and Engineering Chemistry **28** (1936) 1429.
- ²⁹INCROPERA, F. P. and DEWITT, D. P., *Fundamentals of Heat and Mass Transfer*, 5th Edition, Wiley and Sons, USA, 2002.
- ³⁰POLLACK, G. L., Reviews of Modern Physics **41** (1969) 48.
- ³¹XUE, L., KEBLINSKI, P., PHILLPOT, S. R., CHOI, S. U.-S., and EASTMAN, J. A., Int. J. Heat Mass Trans. **47** (2004) 4277.
- ³²MCGAUGHEY, A. J. H. and KAVIANY, M., Phonon transport in molecular dynamics simulations: Formulation and thermal conductivity prediction, in GREENE, G. A., CHO, Y. I., HARTNETT, J. P., and BAR-COHEN, A., editors, *Advances in Heat Transfer*, Volume 39, pp. 169–225, Elsevier, 2006.

- ³³WERDER, T., WALTHER, J. H., JAFFE, R. L., et al., Nanoletters **1** (2001) 697.
- ³⁴K. KADAU, T. C. G. and LOMDAHL, P. S., Los Alamos National Laboratory Reserach Highlight **LA-UR-05-1500** (April 2005).
- ³⁵LI, J., LIAO, D., and YIP, S., Physical Review E **57** (1998) 7259.
- ³⁶P. KUMAR, Z. YAN, L. X. M. G. M. S. B. S.-H. C. S. S. and STANLEY, H. E., Physical Review Letters **97** (2006) 177802(1).
- ³⁷ZANGI, R. and MARK, A. E., Journal of Chemical Physics **120** (2004) 7123.
- ³⁸THOMAS, J. A. and MCGAUGHEY, A. J. H., Journal of Chemical Physics **In Press** (2008).
- ³⁹Y. QUO, N. K. and GODDARD, W. A., Nature **351** (1991) 464.
- ⁴⁰J. H. WALTHER, R. JAFFE, T. H. and KOUMOUTSAKOS, P., J. Phys. Chem. B **105** (2001) 9980.
- ⁴¹BEREZHKOVSKII, A. and HUMMER, G., Physical Review Letters **89** (2002) 064503(1).
- ⁴²R. L. JAFFE, P. GONNET, T. W. J. H. W. and KOUMOUTSAKOS, P., Molecular Simulation **30** (2004) 205.
- ⁴³F. MOULIN, M. D. and PICAUD, S., Physical Review B **71** (2005) 165401(1).
- ⁴⁴HEYES, D. M., *The Liquid State: Applications of Molecular Simulations*, Wiley and Sons, Great Britain, 1998.
- ⁴⁵ZHAO, X. and JOHNSON, J. K., Molecular Simulation **31** (2005) 1.
- ⁴⁶LIU, J. C. and MONSON, P. A., Industrial and Engineering Chemistry Research **45** (2006) 56495656.
- ⁴⁷C. S. LIN, R. Q. ZHANG, S. T. L. M. E. T. F. and WAN, L. J., Journal of Physical Chemistry B **109** (2005) 14183 .
- ⁴⁸SUDIARTA, I. W. and GELDART, D. J. W., Journal of Physical Chemistry A **110** (2006) 10501.
- ⁴⁹FELLER, D. and JORDAN, K. D., Journal of Physical Chemistry A **104** (2000) 9971 .
- ⁵⁰JENSEN, F., *Introduction to Computational Chemistry*, Wiley and Sons, USA, 2006.

⁵¹FORESMAN, J. B. and FRISCH, A., *Exploring Chemistry with Electronic Structure Methods*, Gaussian Inc., Pittsburgh, PA, 1993.

⁵²RUUSKA, H. and PAKKANEN, T. A., Journal of Physical Chemistry B **105** (2001) 9541.

Effect of surface wettability on liquid density, structure, and diffusion near a solid surface

J. A. Thomas and A. J. H. McGaughey^{a)}

Department of Mechanical Engineering, Carnegie Mellon University, Pittsburgh, Pennsylvania 15213

(Received 5 October 2006; accepted 27 November 2006; published online 19 January 2007)

Molecular dynamics and Langevin dynamics simulations are used to elucidate the behavior of liquid atoms near a solid boundary. Correlations between the surface wettability and spatial variations in liquid density and structure are identified. The self-diffusion coefficient tensor is predicted, revealing highly anisotropic and spatially varying mass transfer phenomena near the solid boundary. This behavior affects self-diffusion at a range of time scales. Near a more-wetting surface, self-diffusion is impeded by strong solid-liquid interactions that induce sharp liquid density gradients and enhanced liquid structure. Conversely, near a less-wetting surface, where solid-liquid interactions are weaker, the liquid density is low, the atoms are disordered, and diffusion is enhanced. These findings suggest that altering the wettability of a micro- or nanochannel may provide a passive means for controlling the diffusion of select targets towards a functionalized surface and controlling the reaction rate in diffusion-limited reactions. © 2007 American Institute of Physics. [DOI: [10.1063/1.2424934](https://doi.org/10.1063/1.2424934)]

I. INTRODUCTION

Molecular behavior near material and phase boundaries is complex and difficult to predict. Near an interface (the boundary region separating two fluid domains¹), molecules follow phase diagrams and thermodynamic functions different from either bulk phase.² Near a surface (the region around a solid-solid or solid-liquid boundary), molecular behavior is governed by interactions between the two different materials.^{1,3} The sharp gradients in properties near boundaries are generalized in a continuum-level analysis by using mathematically convenient boundary conditions (e.g., assumptions of no slip, continuous temperature profiles, and continuous concentration profiles). As the scale of engineering systems transitions to the nanoscale, the atomic-level behavior near boundaries assumes a larger role in the overall system behavior.^{4–7} Continuum-based boundary conditions may not be applicable to nanoscale analysis, and an understanding of the actual atomic behavior near surfaces and interfaces is required.

Near a solid-liquid boundary, spatially varying properties are prevalent and have been correlated to the surface wettability.^{8–11} Surface wettability is a measure of the relative strengths of the solid-liquid and liquid-liquid interactions, and is manifest in the contact angle that forms between a liquid droplet and a solid.¹ When liquid atoms experience significant attraction to the surface, the contact angle is less than 90° and the surface is said to be wetting. When liquid dynamics are dominated by liquid-liquid interaction, the contact angle is greater or equal to 90° and the surface is said to be nonwetting.¹² While the notion of a contact angle is not

applicable to liquids confined in micro- or nanochannels, the relationships between wettability, solid-liquid interaction strength, and spatially varying liquid properties are still valid.

Efforts have been made to vary surface wettability to generate tailored transport properties within micro- and nanoscale solid-liquid systems. Hendy *et al.*,¹³ using a model based on the Navier-Stokes equation, analytically demonstrated that patterned surface wettability and the associated variations in slip length can induce complex mixing patterns in microfluidic devices. Similarly, Kuksenok *et al.*,¹⁴ and Kuksenok and Balazs¹⁵ used a lattice Boltzmann model for fluid dynamics to show that surface patterning can be exploited to control the flow and mixing of binary fluids. Using molecular dynamics (MD) simulations, Barrat and Chiaruttini⁵ demonstrated that tailored thermal resistance across a liquid-solid boundary can be obtained by tuning the strength of the solid-liquid interactions.

To complement these investigations and to further understand atomic transport near a solid-liquid boundary, we investigate the self-diffusion of liquid atoms near solid surfaces of different wettability. We begin by using MD simulations to predict and compare the density and structure of liquid atoms near more- and less-wetting solid surfaces. Next, by tracking the atomic positions, we predict survival probabilities, exit probabilities, and atomic mean-squared displacements. We augment the MD data with predictions from Langevin dynamics simulations and identify the spatial dependence of the anisotropic self-diffusion coefficient tensor. Using these findings we present a mechanistic description of liquid self-diffusion (hereto called diffusion) occurring over a range of time scales.

^{a)}Author to whom correspondence should be addressed. Electronic mail: mcgaughey@cmu.edu

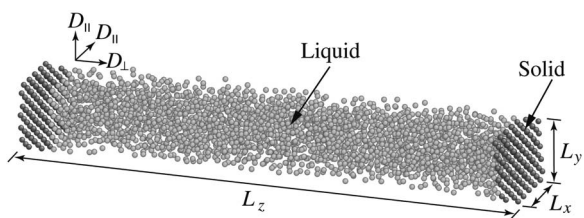


FIG. 1. Simulation cell used to model a solid-liquid boundary. The configuration consists of 2900 atoms with periodic boundary conditions imposed in all three directions. The wide channel generates two independent solid-liquid boundaries.

II. SIMULATION SETUP AND TIME SCALE CONSIDERATIONS

A. Molecular dynamics simulations

The small length and time scales associated with atomic-level dynamics limit the ability of laboratory experiments to resolve nanoscale transport phenomena. Instead, MD simulations, which can access these scales, have become a common tool for modeling atomistic transport.^{16–19} Molecular dynamics is a simulation technique that uses Newton's laws of motion to predict the position and momenta space trajectories of a system of classical particles. The only required inputs are an interatomic potential, which is used to calculate potential energies and forces, and an initial atomic configuration.

The Lennard-Jones (LJ) interatomic pair potential is commonly used in MD simulations of solid-liquid boundaries.^{5,13,20,21} This simple potential allows for the identification of phenomena that may be difficult to resolve in simulations of more complicated materials. For a multicomponent system, the LJ potential can be written as

$$\phi_{\alpha\beta}(r_{ij}) = 4\epsilon_{\alpha\beta} \left[\left(\frac{\sigma_{\alpha\beta}}{r_{ij}} \right)^{12} - \left(\frac{\sigma_{\alpha\beta}}{r_{ij}} \right)^6 \right], \quad (1)$$

where r_{ij} is the distance between atoms i and j , ϵ is the depth of the interaction energy well, and $2^{1/6}\sigma$ is the equilibrium pair separation distance. The subscripts α and β are used to distinguish the interactions between different species.

The MD simulation cell we use to model a solid-liquid boundary is shown in Fig. 1. It contains 2450 liquid atoms and 450 solid atoms with periodic boundary conditions imposed in all three directions. We take the liquid to be argon with $\epsilon_{\parallel}=1.67\times 10^{-21}$ J and $\sigma_{\parallel}=3.4\times 10^{-10}$ m.²² As in previous work on LJ solid-liquid systems, the channel walls are a generic solid modeled with $\epsilon_{ss}=10\epsilon_{\parallel}=10\epsilon$ and $\sigma_{ss}=\sigma_{\parallel}=\sigma$.²¹ The solid atoms are arranged into a face-centered-cubic (fcc) crystal with 5 unit cells in the x and y directions and 4.5 unit cells in the z direction. The noninteger number of unit cells in the z direction generates a midplane where two atoms are fixed at their equilibrium positions to prevent the solid phase from drifting.

The surface wettability is tuned by adjusting the solid-liquid parameter ϵ_{sl} . As shown in Fig. 2, where all the potential energy curves used are plotted, setting ϵ_{sl} to a value greater than 1 makes the solid-liquid interaction stronger than the liquid-liquid interaction (increasing the surface wettability) and setting ϵ_{sl} to a value less than 1 has the opposite

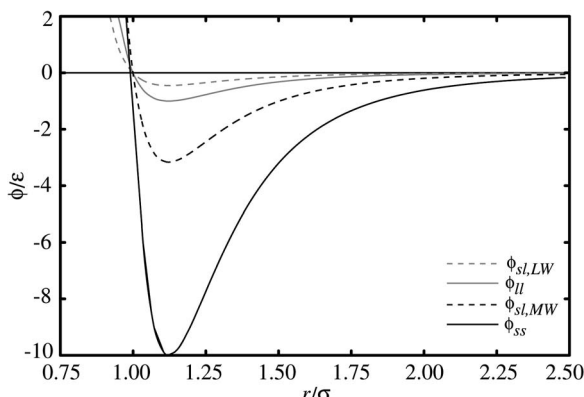


FIG. 2. Comparison between the solid-solid, liquid-liquid, and solid-liquid interaction energies. Interaction strength is a function of distance and is proportional to $\epsilon_{\alpha\beta}$ [see Eq. (1)]. The solid-solid and liquid-liquid interactions in both the more-wetting (MW) and less-wetting (LW) simulations are identical.

effect. In line with other investigations, a more-wetting surface is modeled by setting ϵ_{sl} to $\sqrt{10}\epsilon$.²¹ To model a less-wetting surface, we select an ϵ_{sl} value of 0.45ϵ . In simulations of a liquid droplet in contact with a solid surface, these wetting parameters generate contact angles of approximately 0° (more-wetting) and 85° (less-wetting).¹²

Data are collected from MD simulations run in the NVE (constant mass, volume, and energy) ensemble. The simulations are performed at a temperature of 90 K, above the argon melting temperature of 83.8 K. The equations of motion are integrated using the Verlet leapfrog scheme with a 4.285 fs time step. All interactions are subject to a continuous force/continuous energy cutoff radius of 2.5σ .

The bulk solid zero-pressure lattice constant is 1.552σ . In the simulation cell, the pressure of the liquid atoms on the solid atoms is weaker than that within the solid. This discrepancy causes the lattice constant perpendicular to the solid-liquid surface to naturally be slightly larger than the lattice constant parallel to the surface. We generate an isotropic lattice constant by increasing the parallel-to-surface simulation cell dimensions (L_x and L_y) to 7.830σ , corresponding to a solid lattice constant of 1.566σ .

The 90 K zero-pressure density of the bulk liquid (ρ_0 , obtained from liquid-only simulations) is 1170 kg/m^3 . To ensure that the two surfaces are isolated, we require that the liquid obtain a uniform density of ρ_0 away from the solid surface and maintain this density across the channel centerline. For the more-wetting and less-wetting conditions, we satisfy this condition using L_z values of 63.7σ and 65.7σ , corresponding to channel widths of 15.1 and 15.7 nm. Adjusting L_z has no significant effect on the boundary region density profile.

For analysis purposes, the region inside the channel is virtually partitioned into 0.785σ intervals (one-half of the solid lattice constant) to form a sequence of equal-volume layers parallel to the channel walls. This spatial discretization allows for a direct investigation of the effects of the solid on the behavior of the liquid at various distances from the surface. The implementation of this layering scheme has no influence on the liquid dynamics.

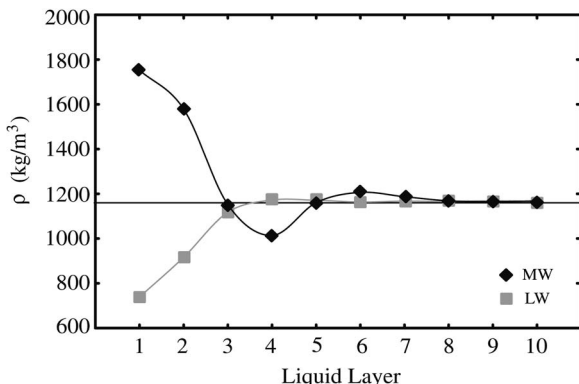


FIG. 3. Density profiles near the more-wetting and less-wetting solids. Guidelines are added to highlight the local minima and maxima. The bulk liquid density (ρ_0 , horizontal line) is recovered in layers far from the solid surface and continues across the channel centerline. Each liquid layer is 0.267 nm (0.785 σ) thick.

B. Atomic diffusion versus atomic migration

As predicted by classical mechanics, the mean-squared displacement (MSD) of a diffusing fluid particle is initially quadratic with respect to time.²³ The curvature of the MSD is important when calculating short-time dynamical quantities such as the memory kernel or velocity autocorrelation function.²³ At longer times, as the statistical nature of the atomic interactions takes over, the MSD becomes linear with a slope proportional to the diffusion coefficient.²⁴ From simulations of bulk liquid argon, we predict that this transition from a quadratic to a linear MSD occurs after 0.21 ps of particle tracking. This result is in good agreement with the transition time predicted by Rahman,²⁵ who performed similar liquid argon simulations.

All mass transport in our system is diffusive. For the purposes of discussion, we make a distinction between atomic diffusion and atomic migration. We use the term atomic diffusion to describe the transport of atoms *within* each liquid layer over a period of 21 ps. This duration is long enough to ensure that our measurements are dominated by a MSD linearly dependent on time, but short enough to ensure that liquid atoms remain in a single layer long enough to measure local mass transfer properties. We use the term “atomic migration” to describe the transport of atoms *across* several layers over a period of 420 ps. These long trials allow us to investigate the behavior of atoms as they exit a layer and disperse throughout the system.

III. DATA COLLECTION AND RESULTS

A. Density profiles

Although the liquid atoms are continually moving, the time-averaged number of atoms in each liquid layer j is well defined. Close to the surface, this mean layer density ρ_j varies as a function of the distance from the solid. Far from the surface, where bulk statistics are recovered, the average number of atoms in each layer is spatially uniform and corresponds to the bulk density. As shown in Fig. 3, the layer-specific densities and the shape of the resulting density profile are strong functions of surface wettability. The layer-specific data presented here and throughout this report were

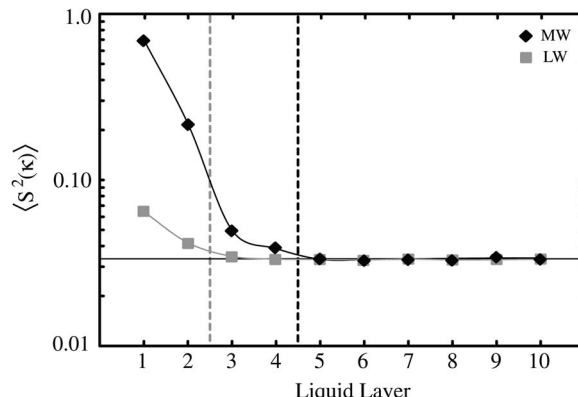


FIG. 4. The liquid structure factor $\langle S^2(\kappa) \rangle$ near the more-wetting and less-wetting surfaces. The solid horizontal line indicates the bulk liquid structure. Near the more- and less-wetting solid, $\langle S^2(\kappa) \rangle$ equals the bulk value in layers 5 and 3, respectively. The dashed lines represent the boundary between solid-moderated and liquid-moderated regions.

obtained by averaging between both solid-liquid boundaries over four data sets, each consisting of 150 independent 21 ps trials. Error bars in all subsequent figures indicate the range of values generated by the four data sets. For many points the error bars are smaller than the data markers.

B. Planar structure factor

The square of the planar structure factor, $\langle S^2(\kappa) \rangle$, was introduced by Lutsko *et al.*²⁶ as a means to quantify the breakdown of crystalline order during melting. The same formulation has been applied by Xue *et al.*²¹ to a confined liquid to measure the layer-by-layer breakdown of liquid ordering near a solid surface. Within liquid layer j , $\langle S^2(\kappa) \rangle$ is given by

$$\langle S_j^2(\kappa) \rangle = \left[\frac{1}{N_j} \sum_i \cos(\kappa \cdot \mathbf{q}_i) \right]^2 + \left[\frac{1}{N_j} \sum_i \sin(\kappa \cdot \mathbf{q}_i) \right]^2, \quad (2)$$

where \mathbf{q}_i is the planar position (x, y) of atom i , N_j is the number of atoms in layer j , and κ is a reciprocal space lattice vector. The summations are taken over all atoms in layer j . When applied to a perfect crystal at zero temperature, $\langle S^2(\kappa) \rangle$ is unity. When applied to a system with noninteracting particles (e.g., an ideal gas), $\langle S^2(\kappa) \rangle$ is zero.

Near the channel walls, the liquid assumes a structure similar to the solid so that κ is taken to be $2\pi/a(\hat{i}+\hat{j})$, where a is the fcc crystal lattice constant. A plot of the structure factor for the ten layers closest to the solid walls for both wettabilities is presented in Fig. 4. The magnitude of $\langle S^2(\kappa) \rangle$ agrees well with the results of Xue *et al.*,²¹ who applied Eq. (2) to a similar more-wetting condition.

Near the more-wetting and less-wetting surfaces, the predicted structure profiles suggest a natural division between regions in which the liquid dynamics are moderated by interactions with the solid and regions in which the liquid dynamics are moderated by interactions with other liquid atoms. These divisions are shown in Fig. 4. In the solid-moderated region, consisting of layers 1–4 in the more-wetting simulation and layers 1 and 2 in the less-wetting simulation, $\langle S_j^2(\kappa) \rangle$ is greater than the bulk liquid value. In

the liquid-moderated region, which consists of all other liquid layers, $\langle S_j^2(\mathbf{k}) \rangle$ is equivalent to the bulk value. Although the imposed 2.5σ cutoff radius prevents direct solid-liquid interactions beyond layer 3, we found that increasing the cutoff to 3.5σ had no significant effect on the shape and magnitude of the predicted density and structure profiles.

C. Survival probability curves and exit probabilities

During tracking, the atoms originally comprising a liquid layer gradually exit into neighboring layers. This behavior generates a time-dependent ratio between the numbers of atoms that originate and remain in a given layer, known as the survival probability P . The time dependence of P is the survival probability curve,²⁷ which for liquid layer j is given by

$$P_j(\tau) = \frac{N_j(\tau)}{N_j(0)}, \quad (3)$$

where τ is time, $N_j(0)$ is the number of atoms in the liquid layer at $\tau=0$, and $N_j(\tau)$ is the number of original atoms remaining in the layer at time τ . Atoms that leave and reenter the layer are not considered in $N_j(\tau)$. We observe that the survival curve decays according to $P_j(\tau) \approx e^{-\tau/\tau_j}$. The layer-specific decay constant τ_j is 2.80 ps in bulklike layers and varies between 1.70 and 3.03 ps in layers closer to the solid where there is diffusion.

Throughout a trial we record both the number of atoms in a given layer that exit towards the solid surface and the number of atoms that exit towards the channel centerline. We then divide these values by $N_j(0)$ to predict layer-specific solid-side exit probabilities $P_{j,s}$ and centerline-side exit probabilities $P_{j,c}$. In the bulklike layers far from either surface, the movement of the atoms is unbiased and $P_s=P_c=0.5$. Closer to the surface, P_s and P_c become unequal as solid interactions and liquid density variations influence atomic dynamics.

D. Atomic diffusion

1. Isotropic versus anisotropic diffusion

In a MD simulation, the diffusion coefficient D_0 of an isotropic system is typically predicted using either the Green-Kubo method or the Einstein method. When using the Green-Kubo method, D_0 is found from the integral of the velocity autocorrelation function.²⁸ In the Einstein method, D_0 of a three-dimensional system is predicted from the MSD of tracked particles by

$$D_0 = \frac{\sum_{i=1}^N \langle |\mathbf{r}_i(\tau) - \mathbf{r}_{i,0}|^2 \rangle}{6N\tau}, \quad (4)$$

where N is the number of atoms in the simulation, \mathbf{r}_0 is the initial position (x, y, z) of atom i , and $\mathbf{r}(\tau)$ its position at time τ .²⁴ The Einstein relation is valid only after the MSD has become linearly dependent on time (see Sec. II). Recognizing this fact, we use Eq. (4) to predict a bulk diffusion coefficient of $4.03 \times 10^{-9} \text{ m}^2/\text{s}$ from liquid-only simulations.

When using either the Green-Kubo or Einstein methods to evaluate D_0 , it is assumed that the diffusing atoms travel

without directional bias and evenly sample the simulation space. However, when modeling transport near surfaces, interfaces, or other systems with spatial gradients, these diffusion formulations are not valid.^{1,11,27,29} The diffusion coefficient becomes directionally dependent (i.e., anisotropic) and must be replaced by the diffusion coefficient tensor, describing diffusion parallel (D_{\parallel}) and perpendicular (D_{\perp}) to the solid surface. Liu *et al.*²⁷ and Wick and Dang²⁹ have developed techniques to predict the diffusion coefficient tensor near a liquid-vapor interface. The approach of Wick and Dang is applied here to the solid-liquid boundary.

2. Diffusion parallel to the surface

Within each liquid layer, the diffusion coefficient parallel to the solid surface, $D_{j,\parallel}$, is found using a modified form of the Einstein method,^{27,29}

$$D_{j,\parallel} = \lim_{\tau \rightarrow \infty} \frac{\langle [\Delta q(\tau)]^2 \rangle_{\mathbf{R}_j}}{4\tau P_j(\tau)}. \quad (5)$$

The numerator within the argument of the limit is the average MSD of liquid atoms that remain in the layer at each time step and is found from

$$\langle [\Delta q(\tau)]^2 \rangle_{\mathbf{R}_j} = \frac{1}{N_j(0)} \sum_{i \in \mathbf{R}_j} [\mathbf{q}_i(\tau) - \mathbf{q}_i(0)]^2, \quad (6)$$

where $\mathbf{R}_j = \mathbf{R}_j(\tau)$ is the subset of the original liquid atoms that remain in layer j at time τ , $\mathbf{q}_i(\tau)$ is the planar position of each atom within the subset \mathbf{R}_j , and $\mathbf{q}_i(0)$ is the initial position of each atom. To account for atoms that exit the layer, $\langle [\Delta q(\tau)]^2 \rangle_{\mathbf{R}_j}$ must be scaled by the survival probability $P_j(\tau)$ at each time step.^{27,29}

As τ increases, \mathbf{R}_j tends towards the null set and the sample size used to evaluate $D_{j,\parallel}$ becomes smaller. To evaluate $D_{j,\parallel}$ while minimizing the noise associated with such small data sets, the argument of the limit in Eq. (5) is averaged over the final 250 time steps (1.1 ps) where $\mathbf{R}_j \geq 5$. To validate this approach, we applied the procedure to layers within a bulk liquid system and found that $D_{j,\parallel}$ was equal to D_0 , as required. The diffusion coefficient parallel to the surface for the first ten layers near the more-wetting and less-wetting solid surfaces is presented in Fig. 5(a).

3. Diffusion perpendicular to the surface

As indicated in Eq. (5), we predict the parallel-to-surface diffusion coefficient by scaling the planar MSD of atoms that remain in the layer by $P_j(\tau)$. The survival probability (which measures displacement normal to the surface) is independent of the planar MSD (which measures displacement parallel to the surface) and serves as a correction factor accounting for atoms that exit the layer. In the direction perpendicular to the surface, the MSD and survival probabilities are correlated (both measure displacement normal to the solid), and applying Eq. (5) in the z direction will bias the predicted diffusion coefficient to low values.

To predict $D_{j,\perp}$ we augment predictions from MD simulations with data from Langevin dynamics.³⁰ Langevin dynamics is a simulation technique that uses a stochastic dif-

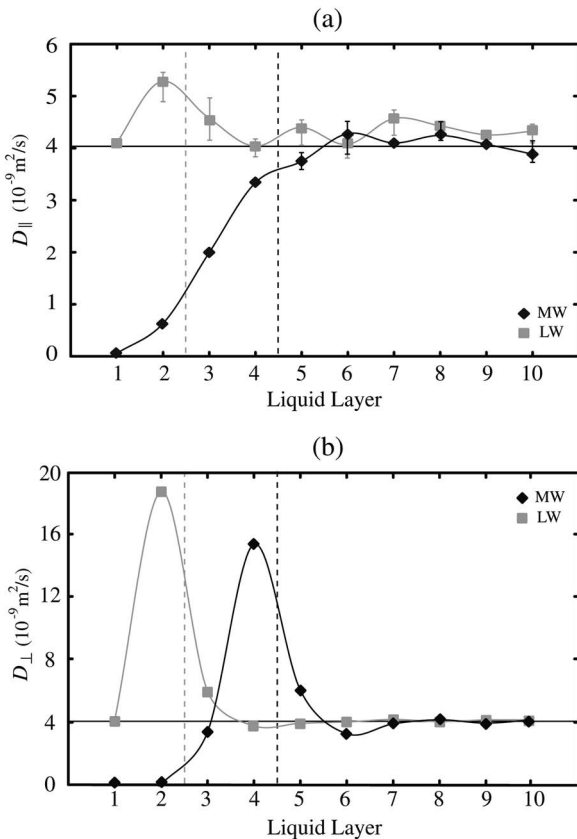


FIG. 5. (a) Diffusion coefficient parallel to the surface. (b) Diffusion coefficient perpendicular to the surface. In both plots, the solid guidelines are added to emphasize critical points and the dashed lines identify the boundary between the solid-moderated and liquid-moderated regions. The error bars represent the range of data predicted from the four data sets. Note that D_{\parallel} and D_{\perp} converge to D_0 (solid horizontal line) in the layers closest to the channel centerline.

ferential equation to approximate the effects of interatomic forces and random thermal motions on atomic dynamics. Although simple Langevin dynamics include neither hydrodynamic coupling nor memory effects, survival probability curves predicted from MD simulation can be reproduced by proper selection of the diffusion coefficient.^{27,29}

In the direction perpendicular to the solid, the Langevin equation takes the form

$$m\ddot{z} = -\frac{k_B T}{D_z}\dot{z} + R(t) - \frac{\partial W(z)}{\partial z}, \quad (7)$$

where k_B is the Boltzmann constant, T is the system temperature, $D_z = D_{\perp}$ is a user-defined diffusion coefficient, $R(t)$ is a stochastic random force, and $W(z)$ is the potential of mean force (PMF). Unlike MD simulations, which assume that particles interact according to classical force fields, the atomic interactions in a Langevin dynamics simulation are modeled as stochastic processes governed by the fluctuation-dissipation theorem through $R(t)$.³⁰ Thus, while particles in a MD simulation follow deterministic position and momentum trajectories, those in a Langevin dynamics simulation follow non-time-reversible trajectories.

The layer-specific PMF is given by

$$W_j = -k_B T \ln\left(\frac{\rho_j}{\rho_0}\right). \quad (8)$$

The spatial derivative of the PMF provides a measure of the local density gradient and is obtained by interpolating the density profiles presented in Fig. 3. We perform this interpolation using a shape-preserving piecewise cubic Hermite interpolating polynomial, which ensures that the derivative is zero at all minima and maxima of the discrete data.³¹

The Langevin dynamics survival curves for each layer are generated using the following procedure.²⁹ A single atom is assigned a random position in a layer of width 0.785σ (corresponding to the width of the MD liquid layers). The atom is then given an initial velocity in a random direction with a magnitude equal to the average velocity predicted from the MD simulations. At each time step, a random force $R(t)$ with

$$\langle R(t) \rangle = 0 \quad \text{and} \quad \langle R(t)R(t') \rangle = \frac{6k_B^2 T^2}{D_z} \delta_{tt'}$$

is applied to the atom in a random direction. Using $R(t)$, the MD-predicted W_j , and a user-defined D_z , Eq. (7) is solved at each time step to calculate the position of the atom over a 5000 time step (21 ps) trial. When the atom is in the layer, the atom-specific survival probability at that time step is 1. If the atom leaves the layer at some point in the trial, the survival probability for the remaining time steps is zero. The atom-specific survival curves from 50 000 independent trials are averaged to form a smooth layer-specific Langevin dynamics survival curve $P_{LD}(\tau)$, which can be compared to the survival curve predicted from the MD trials. From a conceptual standpoint, layers with a high D_z are characterized by quickly decaying survival curves (i.e., a lower τ_j , as discussed in Sec. III).

The inertial effects (i.e., velocity autocorrelation) present in MD simulations lead to faster translational motions than those predicted using simple Langevin dynamics simulation.²⁷ This fact means that the layers used to partition the liquid and generate survival curves from the Langevin dynamics simulation may need to be narrower than those used to partition the MD liquid. Furthermore, any comparisons between the two simulation techniques should only be made after the atomic MSD measured from the MD simulation becomes linear.

The D_z term in Eq. (7) for a given layer is adjusted until the difference between $P_{LD}(\tau=9.6 \text{ ps})$ and $P(\tau=9.6 \text{ ps})$ is less than 0.005.²⁹ Once this condition is satisfied, a second comparison is made between $P_{LD}(\tau=16.8 \text{ ps})$ and $P(\tau=16.8 \text{ ps})$. If this second comparison yields a difference greater than 0.005, the width of the Langevin dynamics simulation layer is reduced and D_z is reevaluated. Upon obtaining suitable agreement at times of 9.6 and 16.8 ps, D_z is recorded as D_{\perp} and the comparison sequence is repeated for the next liquid layer. The exact choice of comparison times, provided they are greater than 0.21 ps (the linear-quadratic transition time presented in Sec. II), was found to have little effect on the value of D_z that generated the best fit to the MD data. The predicted diffusion

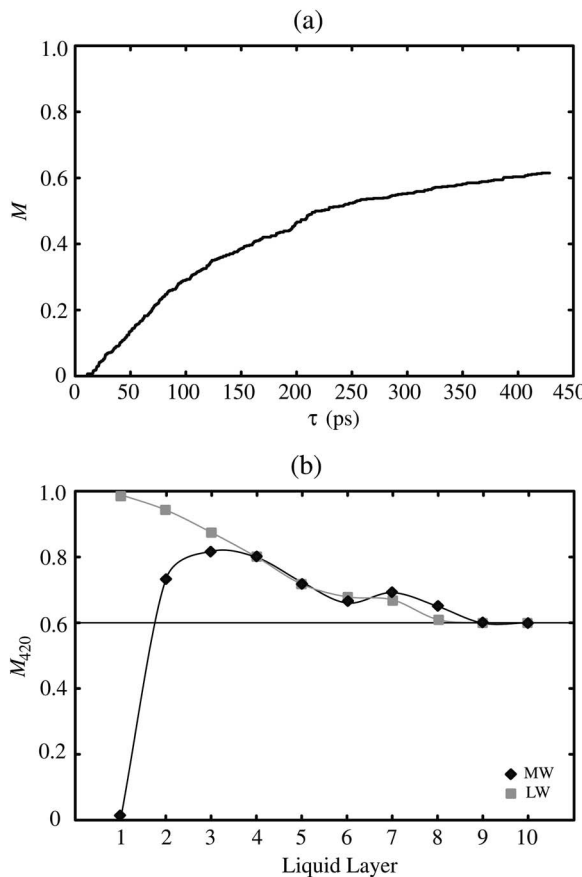


FIG. 6. (a) Time evolution of M for atoms migrating across four bulk liquid layers. (b) Atomic migration across four liquid layers in the direction away from the solid-liquid boundary. The migration fraction M_{420} identifies the fraction of atoms successfully migrating from the origin layer (layer number) to the destination layer (layer number +4) over 420 ps trials. The horizontal line identifies M_{420} for a layer in bulk liquid.

coefficient perpendicular to the surface for the first ten layers near the more-wetting and less-wetting solid surfaces is presented in Fig. 5(b).

E. Atomic migration

As introduced in Sec. II, we use the term atomic migration to describe the aggregate movement of atoms over long times across multiple liquid layers. We generate migration statistics by identifying the atoms within an origin layer, tracking their positions as they diffuse through the system, and recording the time each atom arrives at a specified destination layer. Instead of capturing local liquid dynamics, migratory statistics predict the integrated effect of spatially varying properties on atomic mass transfer.

Random interatomic collisions and varied atomic velocities reduce the probability that all atoms from the origin layer will simultaneously arrive at the destination layer. Instead, the fraction of atoms successfully migrating, M , from an origin layer to a destination layer is a function of time [i.e., $M=M(\tau)$]. As presented in Fig. 6(a), which presents $M(\tau)$ for atoms migrating across four bulk liquid layers, $M(\tau)$ monotonically increases from zero. The shape of $M(\tau)$ results from the number of diffusion paths available to migrating atoms. Some atoms may exit the origin layer and

follow a direct path to the destination layer with few collisions or interactions. Other atoms may take less direct paths or cross the intermediate layers many times in the tracking period. Although all atoms from the origin layer will eventually reach the destination layer, the long trials required to observe such completion are computationally impractical. Over the 420 ps trials used here, 60% of atoms successfully migrate across four bulk layers, a fraction sufficient to resolve relevant trends.

To investigate the effects of the solid surface on liquid migration, we measure the ability of atoms originating near the surface to migrate across four liquid layers in the direction towards the channel centerline. As presented in Fig. 6(b), the fraction of atoms successfully migrating over a 420 ps trial, M_{420} , from layer j (the origin layer) to layer $(j+4)$ (the destination layer) is a function of both original distance from the solid and surface wettability. These migration data were obtained by averaging between both solid-liquid boundaries over ten independent trials. As expected, for bulklike origin layers far from the surface, M_{420} approaches the bulk value.

IV. ANALYSIS AND INTERPRETATION

A. Density and structure

The atoms in the liquid layer closest to the more-wetting surface (layer 1) assume a density and structure closely resembling the solid walls. These layer 1 atoms do not diffuse and have equilibrium positions mimicking the fcc lattice. Across layers 2–4, the movement and structure of the liquid atoms become increasingly random and, as presented in Fig. 4, the structure factor decreases monotonically to its bulk value. As shown in Fig. 3, the liquid density decreases in the direction away from the solid, reaching a minimum of $0.87\rho_0$ in layer 4, then settles to ρ_0 by layer 8. The density minimum present in layer 4 is explained as follows. In layers 1–3 near the more-wetting solid, strong attractive forces draw liquid atoms towards the solid, increasing the local liquid density. The attractive force that the solid atoms exert on the liquid atoms decreases with distance, and in liquid layers beyond the influence of the solid, the liquid atoms are repelled by the dense assembly of liquid atoms near the surface. In the current configuration, this repulsion generates a region of low liquid density in layer 4.

In the less-wetting system, the liquid-liquid interactions are stronger than the solid-liquid interactions. Thus, rather than experiencing a strong attraction towards the solid, liquid atoms are drawn towards other liquid atoms and away from the surface. This behavior generates the density profile presented in Fig. 3, in which the density increases monotonically from $0.63\rho_0$ to ρ_0 in the direction towards the channel centerline. Although the structure factor in the first two liquid layers is above the bulk value, all liquid atoms readily diffuse.

B. Diffusion within the layers

1. Diffusion perpendicular to the surface

Spatially varying anisotropic diffusion coefficient tensors have been predicted in MD simulations of liquid-vapor

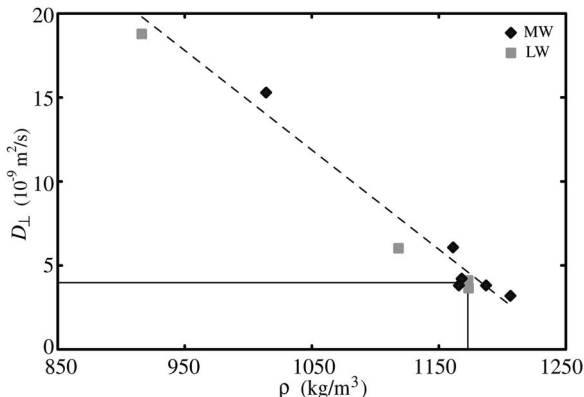


FIG. 7. Correlation between D_{\perp} and density in liquid-moderated regions near more- and less-wetting solids. A best-fit line is added to highlight the trend. Included are data from the last layer of the solid-moderation region; these transition layers assume characteristics of both regions. The solid horizontal and vertical lines identify D_0 and ρ_0 . The intersection of these two lines corresponds to bulk conditions.

water interfaces.^{27,29} Wick and Dang²⁹ explain this behavior using a vacancy model where diffusion is enhanced in regions of low density. As presented in Figs. 5(a) and 5(b), spatially varying diffusion coefficients exist near the LJ solid-liquid boundary. In agreement with the vacancy model, and as presented in Fig. 7, D_{\perp} is correlated to density in the liquid-moderated regions in both the more- and less-wetting simulations. Although a similar correlation between D_{\parallel} and density likely exists, the uncertainty in our data [see Fig. 5(a)] is too great to make a definite conclusion.

The linear correlation between D_{\perp} and density does not persist into the the solid-moderated region (not present in liquid-vapor interface systems). This is because the atomic dynamics within these regions are also affected by direct solid-liquid interactions. Thus, although liquid density variations will partially affect atomic mobility, mass transfer within the solid-moderated regions is impeded by the attractive force pulling liquid atoms towards the surface. This argument is consistent with our predictions. For example, layers 3 and 5 in the more-wetting simulation have similar densities, but D_{\perp} in layer 3 (a solid-moderated layer) is significantly lower than D_{\perp} in layer 5 (a liquid-moderated layer). Similarly, while the density in layer 1 near the less-wetting system is only $0.63\rho_0$, D_{\perp} is comparable to D_0 .

In the outermost solid-moderated layer (layer 4 in the more-wetting simulation and layer 2 in the less-wetting simulation), the solid-liquid interaction force is weak and D_{\perp} becomes correlated to density (see Fig. 7). While this transition to density-moderated diffusion is expected, the D_{\perp} maxima (see Fig. 5) are surprising. The underlying physics causing this behavior are not yet clear. However, we expect that the liquid atoms in this region have long velocity auto-correlations perpendicular to the surface, causing rapid movement into either the solid-moderated region or the liquid-moderated region.

Although governed by different mechanisms, liquid diffusion in both the solid- and liquid-moderated regions can be further understood by considering the layer-specific exit probabilities (see Sec. III) and the local liquid density gradient (as predicted by the PMF). Observe in Fig. 8 that a strong

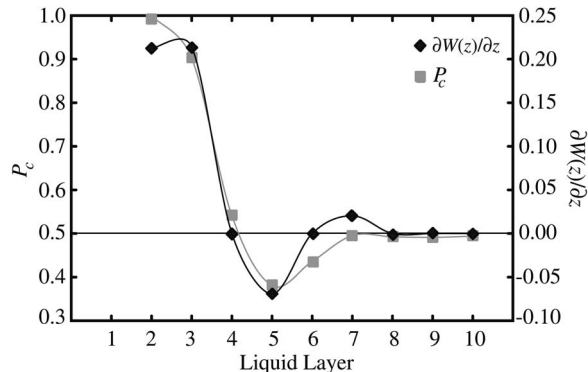


FIG. 8. Correlation between the centerline-side exit probability P_c and the derivative of the PMF for the more-wetting solid. The horizontal line at $P_c=0.5$ corresponds to bulklike layers where $\partial W(z)/\partial z=0$ and movement is unbiased.

correlation exists between the centerline-side exit probability P_c and the derivative of the PMF [$\partial W_j(z)/\partial z$] used in the Langevin dynamics simulations. When a layer has a positive $\partial W(z)/\partial z$, implying that the local density is decreasing in the direction of the centerline, the atoms in that layer are likely to exit away from the solid surface (i.e., $P_c > P_s$). Conversely, when $\partial W(z)/\partial z$ is negative, meaning the local atom density is decreasing in the direction of the solid, atoms in the layer are likely to exit towards the solid surface (i.e., $P_s > P_c$). Thus, although atoms in layers with enhanced D_{\perp} more readily diffuse perpendicular to the solid, the local PMF and associated density gradient dictate the direction these atoms are likely to travel.

2. Diffusion parallel to the surface

As discussed above, D_{\parallel} deviates from D_{\perp} near a liquid-vapor water interface.^{27,29} Liu *et al.*²⁷ qualitatively attribute the anisotropic mass transfer to variations in liquid structure that naturally arise near a boundary. As presented in Fig. 9, D_{\parallel} deviates from D_{\perp} in our solid-liquid simulations. And, in agreement with the argument presented by Liu *et al.*, this behavior is related to variations in liquid structure. Observe in Fig. 10 that a strong correlation between D_{\parallel} and $\langle S^2(\mathbf{k}) \rangle$ is

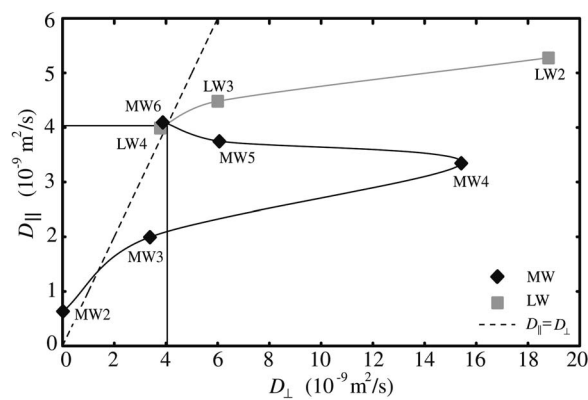


FIG. 9. Anisotropy of the diffusion coefficient tensor near the more- and less-wetting surfaces. In most layers, D_{\perp} is greater than D_{\parallel} , implying that diffusion perpendicular to the surface is enhanced more than diffusion parallel to the surface. The dashed line represents isotropic diffusion. The solid lines correspond to D_0 of the bulk liquid.

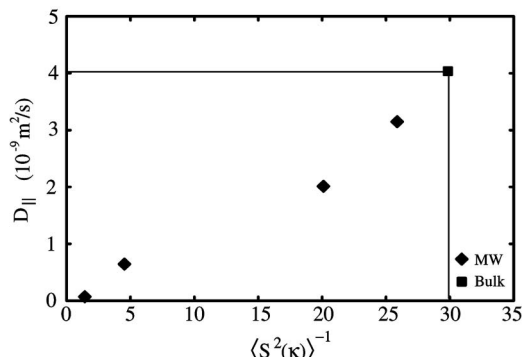


FIG. 10. Correlation between D_{\parallel} and $\langle S^2(\kappa) \rangle^{-1}$ for liquid layers 1–4 near the more-wetting solid. Although enhanced ordering exists within layer 1 near the less-wetting surface, the low liquid density limits the impact of the liquid structure on D_{\parallel} . The horizontal and vertical lines correspond to bulk D_0 and the bulk $\langle S^2(\kappa) \rangle^{-1}$. The intersection identifies bulk conditions.

present near the more-wetting surface. This trend is expected: when $\langle S^2(\kappa) \rangle$ is high, the dense, crystal-like structure present in these layers should reduce the planar mobility of the liquid atoms. Since the magnitude of the liquid structure factor (which governs D_{\parallel}), the strength of the direct solid-liquid interactions, and the density (which governs D_{\perp}) are not strongly coupled, an anisotropic diffusion coefficient tensor is generated within the solid-moderated region. The differences between D_{\parallel} and D_{\perp} continue into the first liquid-moderated layer. Although direct solid-liquid interactions are negligible at this position, the lingering effects of liquid structure may damp diffusion parallel to the surface and generate the continued anisotropy.

C. Migration across the layers

As discussed in Sec. III, liquid atoms in a bulk system diffuse without directional bias, and the fraction of atoms that successfully migrate across four layers during a 420 ps trial, M_{420} , is 0.60. Because liquid atoms cannot diffuse into the solid surface, migration of liquid atoms near the solid-liquid boundary is naturally biased towards the channel centerline. Thus, as presented in Fig. 6(b), M_{420} for atoms originating near either the more-or less-wetting surface is greater than the bulk value.

Although both solids bias migration towards the channel centerline, M_{420} is a function of distance from the solid and surface wettability. Near the less-wetting solid, the layer densities are low and the solid-liquid interactions pulling atoms towards the surface are weak compared to the liquid-liquid interactions pulling atoms towards the bulk liquid. The result is a high M_{420} in layers 1 and 2 with nearly 100% of the atoms successfully migrating four layers towards the channel centerline. The increasing density (which raises the atomic collision frequency) and the growing number of diffusion paths available to atoms originating in layers 3–6 causes M_{420} to decrease monotonically to the bulk value.

As discussed, atoms in layer 1 near the more-wetting solid do not diffuse and M_{420} is zero. Across layers 2 and 3, the average solid-liquid interaction force becomes smaller while the density gradient $\partial W(z)/\partial z$ decreases in the direction away from the solid surface. These trends enhance mi-

gration towards the channel centerline and cause M_{420} to obtain a local maxima in layer 3. Across layers 4–6, the density increases in the direction towards the channel centerline, impeding migration away from the solid. Furthermore, the increased number of diffusion paths available to atoms originating within these layers cause M_{420} to decrease and to obtain a local minimum in layer 6. In layers 7 and beyond, $\partial W(z)/\partial z$ again becomes positive (meaning migration towards the channel centerline is encouraged) and M_{420} decays to the bulk value.

V. SUMMARY AND DISCUSSION

We have investigated the effect of surface wettability on liquid structure, mobility, and diffusion near a solid surface using molecular dynamics simulations. As presented in Figs. 3 and 4, the density and structure of a liquid near a solid are dependent on the surface wettability. Near the more-wetting surface, both the liquid structure factor and density are well above bulk liquid values. Near the less-wetting surface, the liquid assumes enhanced structure but the density is low. The structure factor profiles suggest a natural division between a liquid region that is moderated by solid-liquid interactions and a liquid region that is moderated by liquid-liquid interactions.

Using a modified mean-squared displacement relation and Langevin dynamics simulations, we predicted the diffusion coefficient tensor near both surfaces. The diffusion coefficient tensor, which describes diffusion parallel [Fig. 5(a)] and perpendicular [Fig. 5(b)] to the solid-liquid boundary, is spatially varying and is a strong function of surface wettability. In the liquid-moderated regions in both more- and less-wetting simulations, where solid-liquid interactions are negligible, a correlation between density and D_{\perp} exists (see Fig. 7). This trend agrees with predictions from other simulations of liquid-vapor interfaces.^{27,29} As presented in Fig. 10, a correlation between D_{\parallel} and liquid structure is present in layers near the more-wetting solid. This trend between D_{\parallel} and structure, also predicted in previous simulations of the liquid-vapor interface,^{27,29} seems sensible; the enhanced ordering in these layers should reduce the planar mobility of the liquid atoms. Because D_{\parallel} and D_{\perp} are governed by different phenomena, an anisotropic diffusion coefficient tensor is generated near the surface. As seen in Fig. 9, the directional dependence of the diffusion coefficients (represented as the ratio of D_{\parallel} to D_{\perp}) is a function of surface wettability.

We also investigated the effects of surface wettability on atomic migration, the diffusion of atoms across many liquid layers. As presented in Fig. 6, the fraction of atoms successfully migrating from an origin layer to a destination layer is a function of time. The shape of this curve results from the variety of diffusion paths available to migrating atoms. Over a certain tracking period, the fraction of liquid atoms successfully migrating away from the solid surface is a function of surface wettability and distance from the solid. Observe in Fig. 6(b) that atoms near a solid of either wettability are likely to diffuse towards the channel centerline. However, due to significant solid-liquid interactions, liquid atoms near

the more-wetting solid are less likely to migrate towards the centerline compared to atoms near the less-wetting surface.

The presence of an anisotropic diffusion tensor and the effects of surface wettability on atomic migration may be used to generate tailored mass transport properties. For example, tuning the surface wettability of the channel walls in diffusion-limited micro- and nanofluidic reactions may be one way to obtain desired reaction rates. Similarly, the surface wettability could be altered to ensure that targets quickly migrate towards certain functional surfaces while other targets, on account of the anisotropic diffusion coefficient tensor, are led to alternative reaction sites.

In molecular liquids, such as water and organic solvents, ordering and density variations are further enhanced by hydrogen bonding and electrostatic forces.³² In preliminary investigations, such interactions have been shown to generate a spatially varying anisotropic diffusion coefficient tensor.⁸ However, a high spatial resolution, mechanistic investigation into the transport properties (diffusion coefficient, viscosity, and thermal conductivity tensor) of liquid water near a solid surface must still be performed.

- ¹J. Berthier and P. Silberzan, *Microfluids for Biotechnology* (Artech House, Boston, 2006).
- ²M. Wortis, *Ordering in Two Dimensions* (North Holland, New York, 1980).
- ³R. F. Hainsey, R. Gangwar, J. D. Shindler, and R. M. Suter, Phys. Rev. B **44**, 3365 (1991).
- ⁴G. Arya, H.-C. Chang, and E. J. Maginn, Mol. Simul. **29**, 697 (2003).
- ⁵J.-L. Barrat and F. Chiaruttini, Mol. Phys. **101**, 1605 (2003).
- ⁶A. R. Abramson, C.-L. Tien, and A. Majumdar, J. Heat Transfer **124**, 963 (2002).
- ⁷M. Angadi, T. Watanabe, A. Bodapati, X. Xiao, O. Auciello, J. A. Carlisle, J. A. Eastman, P. Kebinski, P. K. Schelling, and S. R. Phillipot,

J. Appl. Phys. **99**, 114301 (2006).

⁸S. H. Lee and P. J. Rossky, J. Chem. Phys. **100**, 3334 (1994).

⁹M. Cieplak, J. Koplik, and J. R. Banavar, Phys. Rev. Lett. **86**, 803 (2001).

¹⁰C.-J. Yu, A. G. Richter, J. Kmetko, S. W. Dugan, A. Datta, and P. Dutta, Phys. Rev. E **63**, 021205 (2001).

¹¹L. P. Faucheuax and A. J. Libchaber, Phys. Rev. E **49**, 5158 (1994).

¹²S. Maruyama, T. Kurashige, S. Matsumoto, Y. Yamaguchi, and T. Kimura, Microscale Thermophys. Eng. **2**, 49 (1998).

¹³S. C. Hendy, M. Jasperse, and J. Burnell, Phys. Rev. E **72**, 016303 (2005).

¹⁴O. Kuksenok, J. M. Yeomans, and A. C. Balazs, Phys. Rev. E **65**, 031502 (2002).

¹⁵O. Kuksenok and A. Balazs, Phys. Rev. E **68**, 011502 (2003).

¹⁶A. J. H. McGaughey, M. I. Hussein, E. S. Landry, M. Kaviany, and G. M. Hulbert, Phys. Rev. B **74**, 104304 (2006).

¹⁷A. I. Skoulios and D. S. Sholl, J. Phys. Chem. B **105**, 3151 (2001).

¹⁸D. Bedrov and G. D. Smith, J. Chem. Phys. **113**, 8080 (2000).

¹⁹K. Meier, A. Laesecke, and S. Kabelac, J. Chem. Phys. **121**, 9526 (2004).

²⁰P. Kebinski and J. Thomin, Phys. Rev. E **73**, 010502(R) (2006).

²¹L. Xue, P. Kebinski, S. R. Phillipot, S. U.-S. Choi, and J. A. Eastman, Int. J. Heat Mass Transfer **47**, 4277 (2004).

²²N. W. Ashcroft and N. D. Mermin, *Solid State Physics* (Saunders College, Fort Worth, 1976).

²³B. J. Berne and G. D. Harp, Adv. Chem. Phys. **17**, 63 (1970).

²⁴D. A. McQuarrie, *Statistical Mechanics* (Viva Books, New Delhi, 2005).

²⁵A. Rahman, Phys. Rev. **136**, A405 (1964).

²⁶J. F. Lutsko, D. Wolf, S. R. Phillipot, and S. Yip, Phys. Rev. B **40**, 2841 (1989).

²⁷P. Liu, E. Harder, and B. J. Berne, J. Phys. Chem. B **108**, 6595 (2004).

²⁸R. Zwanzig, Annu. Rev. Phys. Chem. **16**, 67 (1965).

²⁹C. D. Wick and L. X. Dang, J. Phys. Chem. B **109**, 15574 (2005).

³⁰M. P. Allen and D. J. Tildesley, *Computer Simulation of Liquids* (Oxford University Press, New York, 1987).

³¹C. Moler, *Numerical Computing with Matlab* (Society for Industrial and Applied Mathematics, Philadelphia, 2004).

³²L. Cheng, P. Fenter, K. L. Nagy, M. L. Schlegel, and N. C. Sturchio, Phys. Rev. Lett. **87**, 156103 (2001).

December 20, 2007

**Density, distribution, and orientation of water molecules inside
and outside carbon nanotubes**

J. A. Thomas and A. J. H. McGaughey*

Department of Mechanical Engineering

Carnegie Mellon University

Pittsburgh, PA 15213 USA

*Address all correspondence to mcgaughey@cmu.edu

Abstract

The behavior of water molecules inside and outside 1.1, 2.8, 6.9, and 10.4 nm diameter armchair carbon nanotubes (CNTs) is predicted using molecular dynamics simulations. The effects of CNT diameter on mass density, molecular distribution, and molecular orientation are identified for both the confined and unconfined fluids. Within 1 nm of the CNT surface, unconfined water molecules assume a spatially varying density profile. The molecules distribute non-uniformly around the carbon surface and have preferred orientations. The behavior of the unconfined water molecules is invariant with CNT diameter. The behavior of the confined water, however, can be correlated to tube diameter. Inside the 10.4 nm CNT, the molecular behavior is indistinguishable from that of the unconfined fluid. Within the smaller CNTs, surface curvature effects reduce the equilibrium water density and force water molecules away from the surface. This effect changes both the molecular distribution and preferred molecular orientations.

I. Introduction and motivation

Advances in carbon nanotube (CNT) fabrication techniques and new experimental and theoretical investigations into fluid flow through ultra-confined geometries have generated interest in nanofluidic based sensors and devices.¹ Yun *et al.* recently fabricated stable and axially-aligned CNT arrays with an unprecedented length of 1 cm.² Li *et al.* built CNT networks containing well-aligned and uniform CNT Y-junctions with controllable branch and spur dimensions.³ Skouidas *et al.*⁴ and Holt *et al.*⁵ both report anomalously high mass flow rates through CNT membranes, while Shim *et al.* functionalized CNT surfaces to be biocompatible and capable of recognizing proteins.⁶

The thermophysical and mass transport properties of such liquid-CNT systems — information necessary for device design and optimization — are related to the liquid-carbon intermolecular interactions and the associated surface wettability. These wetting characteristics can be implicitly incorporated into continuum-based analysis techniques by selecting appropriate boundary conditions for the mass, momentum, and energy transfer equations. For transport analysis at the nanoscale, however, where continuum assumptions break down,^{7–9} explicit modeling of individual molecules is necessary to predict system performance.

The small length and time scales associated with atomic-level dynamics limit the ability of laboratory experiments to resolve liquid-CNT interactions. Molecular dynamics (MD) simulation, which can access these scales, has emerged as an alternative tool for studying such nanoscale transport phenomena.^{10–18} In an MD simulation, intermolecular potential functions and the Newtonian equations of motion are used to calculate the position and momentum space trajectories of a system of molecules. The molecular behavior can then be used to predict thermophysical properties and study transport phenomena.

Predictions from MD simulations have indicated that the behavior of liquid water both inside and outside of CNTs is strongly influenced by interactions with the carbon atoms.^{13–16} Walther *et al.* predicted a spatially-varying density profile and non-uniform molecular orientation distribution in water outside a 12.5 nm single-walled CNT.¹³ Similar variations in water density were predicted by Choudhury for water-C₆₀ suspensions.¹⁴ In investigating flow through single-walled CNTs, Kotsalis *et al.* predicted enhanced liquid ordering near the interior carbon surface and low liquid densities across the channel centerline.¹⁵ Non-uniform interior water density profiles that vary as a function of CNT diameter were also reported by Hanasaki and Nakatani.¹⁶

To compliment these investigations and assist in the design of future nanofluidic devices, here

we use MD simulations to systematically investigate the effect of CNT diameter on the density, distribution, and orientation of water molecules inside and outside single-walled 1.1, 2.8, 6.9, and 10.4 nm diameter armchair CNTs [with chirality vectors of (8,8), (20,20), (50,50), and (75,75)]. We go beyond previously reported simulation results by elucidating the specific molecular interactions responsible for the spatially varying liquid properties. We also identify how, in addition to liquid water density, tube diameter can passively tune the distribution and orientation of confined water molecules. Such information may be useful in understanding how water flows through and around CNTs, and how heat is transferred between a CNT and a surrounding liquid.

We begin by discussing the water-water and water-carbon intermolecular potential functions and the MD simulation techniques used to analyze the CNT-water system. Next, we study the effect of CNT diameter on liquid density both inside and outside the CNT. We then identify the effect of CNT diameter on the distribution of water molecules near the CNT surface and correlate these results to previously reported experimental measurements. Finally, we identify the molecular orientation distribution of water molecules both inside and outside the CNT, and discuss how the orientation is affected by tube diameter.

II. Molecular dynamics simulations set-up

A. Water potential

We model water-water interactions using the TIP5P potential.¹⁹ In TIP5P, each water molecule consists of one electrostatically-neutral oxygen atom, two positively-charged hydrogen atoms, and two negatively-charged but massless interaction sites. The relative positions of the oxygen and hydrogen atoms correspond to known molecular structure data, while the positions of the charged interaction sites were tuned to reproduce the experimentally-observed properties of bulk water.¹⁹ The three atoms and two interaction sites are fixed with respect to a local basis set and each molecule has zero net-charge.

The interaction between two water molecules, a and b , is a combination of one Lennard-Jones (LJ) interaction between the oxygen atoms, and sixteen electrostatic interactions between the two hydrogen atoms and two charge sites on each molecule:

$$\phi_{ab} = 4\epsilon_{OO} \left[\left(\frac{\sigma_{OO}}{r_{OO}} \right)^{12} - \left(\frac{\sigma_{OO}}{r_{OO}} \right)^6 \right] + \sum_{i=1}^4 \sum_{j=1}^4 \frac{1}{4\pi\epsilon_o} \frac{q_i q_j}{r_{ij}}. \quad (1)$$

In Eq. (1), ϵ_{OO} and σ_{OO} are the LJ parameters for the oxygen-oxygen interaction, r_{OO} is the

oxygen-oxygen separation distance, q_i is the charge on site i of molecule a , q_j is the charge on site j of molecule b , ϵ_0 is the permittivity of free space, and r_{ij} is the charge site separation distance. We use the potential parameters and charges recommended by the potential developers.¹⁹

As recommended in the original TIP5P implementation, we subject all molecular interactions to a 0.9 nm oxygen-oxygen cutoff radius at which interactions are truncated. It has been asserted that applying a spherical cut-off to a water model with long-range electrostatic interactions adversely effects system energetics and density.²⁰ To address this point, in Fig. 1 we show the net intermolecular force versus oxygen separation distance between two TIP5P water molecules in an equilibrated simulation of 512 molecules at a temperature of 298 K and a pressure of 1 atm. A range of forces (illustrated by the shaded envelope on the plot) are measured at each separation distance, and are related to the variety of relative orientations accessible to the molecules. The mean effective intermolecular force at each distance is also shown. For two molecules separated by more than 0.7 nm, the force envelope decays as $1/(r_{OO})^4$, characteristic of the interaction between two permanent dipoles.²¹ The mean effective force at such separation distances (solid line) decays as $1/(r_{OO})^7$, consistent with the oxygen-oxygen LJ interaction. Consequently, the total force between two molecules, which is used to integrate the equations of motion, decays much more rapidly than the individual Columbic forces [which decay as $1/(r_{OO})^2$]. This rapid decay is why, even with truncating the individual long-range Coulomb interactions, the TIP5P model can accurately reproduce water statistics.²² Along with the domination of nearest neighbor interactions on overall dynamics, this trend also explains why others have been able to successfully model water using even smaller truncation spheres.²³ Such a rapid decay in intermolecular forces will not be present in ionic systems where individual molecules have a non-zero charge.

B. Carbon-water potential

We model carbon-water interactions using the LJ potential recommended by Werder *et al.*:

$$\phi_{CO} = 4\epsilon_{CO} \left[\left(\frac{\sigma_{CO}}{r_{CO}} \right)^{12} - \left(\frac{\sigma_{CO}}{r_{CO}} \right)^6 \right], \quad (2)$$

where r_{CO} is the carbon-oxygen separation distance, $\epsilon_{CO}(= 1.11 \times 10^{-21} \text{ J})$ is the depth of the LJ energy well, and $\sigma_{CO}(= 0.319 \text{ nm})$ is the LJ length scale.²⁴ A 0.9 nm cutoff is applied to the carbon-oxygen interactions. Although the CNT-water contact angle is not well defined from experiment,²⁵ the recommended parameters accurately reproduce the observed wetting behavior of water on graphite.

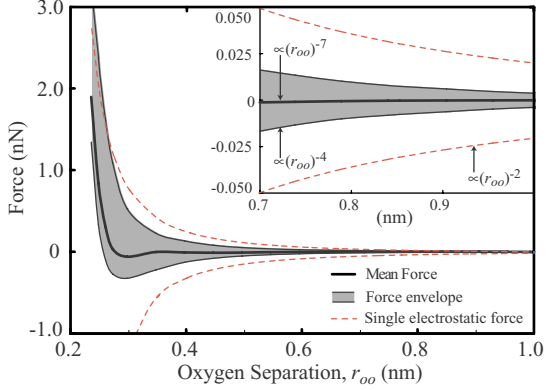


Figure 1: (color online) Intermolecular force versus oxygen separation distance between two water molecules in an equilibrated simulation of 512 molecules at a temperature of 298 K and a pressure of 1 atm. The gray envelope represents the range of forces predicted at each separation distance. The solid line is the mean force at each distance. Inset: Force envelope and mean force at separation distances greater than 0.7 nm. At these separations, the force envelope decays as $1/(r_{OO})^4$, characteristic of a permanent dipole-permanent dipole interaction. The mean effective force is related to the oxygen-oxygen LJ interactions and decays as $1/(r_{OO})^7$.

The LJ potential is a model of atomic repulsion due to overlapping electron orbitals and atomic attraction due to atomic dipole dispersion (i.e. van der Waals forces). The carbon atoms in a CNT are sp^2 hybridized, meaning that each carbon has one delocalized π -electron. Thus, in addition to carbon-oxygen LJ interactions and possible carbon-hydrogen interactions,²⁶ water molecules may also interact with this delocalized electron. Previous MD simulations have demonstrated that the electrostatic interactions between a CNT and water are negligible compared to the van der Waals interactions, suggesting that electron-water interactions may be unimportant.²⁷ However, additional *ab initio* potential development and more research into the CNT-water contact angle will determine if more sophisticated intermolecular potentials are necessary.

For computational efficiency, the carbon atoms within each simulation cell are fixed. In an extension of our previously reported work on monatomic LJ solid-fluid interfaces,²⁸ we found that fixing the solid atoms had no detectable effect on the density, distribution, and diffusion characteristics of the interfacial liquid. Others have reported that fixing the carbon atoms has little effect on the dynamics of adjacent water.²⁴

Although stable single-walled nanotubes with diameters greater than 1.5 nm are difficult to fabricate, we have found that molecular behavior near multi-walled nanotubes is indistinguishable

from that near single-walled CNTs due to the short range of the carbon-water interactions. Thus, the results from our single-walled nanotube simulations can be applied to multi-walled nanotubes with similar interior or exterior dimensions.

C. Simulation implementation and data collection

Our simulations are performed in the *NVT* ensemble (constant mass, volume, and temperature). The rotational dynamics of the water molecules are modeled using the quadterion method and translational dynamics are integrated using the Verlet leapfrog scheme with a 0.5 fs timestep.¹¹ The temperature is maintained at 298 K using a Berendsen thermostat and the volume of the simulation cell is tuned to recover a water density of 1000 kg/m³ in regions far from the carbon surface. Periodic boundary conditions are imposed in all three directions.

To predict the equilibrium water density inside the 1.1, 2.8, and 6.9 nm CNTs, we simulated an open-ended sample of each nanotube in a large water bath at a temperature and pressure of 298 K and 1 atm. The bath density away from the tube was maintained at 1000 kg/m³ and water molecules were able to freely diffuse across the open ends of the tube. After 250 ps, the number of molecules enclosed inside the tube became steady in time, allowing us to determine the equilibrium density. The CNTs used to generate all of the subsequently reported data span the entire simulation cell (thereby isolating the confined and unconfined fluids) and were initially filled with the number of molecules corresponding to this equilibrium density. Simulating the 10.4 nm CNT in a large water bath is computationally impractical. As such, we determined the equilibrium internal water density by predicting the pressure inside a 64 nm³ cube centered within a nanotube of this size that spans the simulation cell. The number of molecules inside the CNT was tuned to recover a pressure of 1 atm within the cube. Applying this same technique to the 6.9 nm CNT generated an equilibrium water density within 1% of that predicted using the water-bath method.

In Fig. 2(a) we present a snapshot of the 2.8 nm CNT. We virtually partition the water into a sequence of shells concentric to the carbon surface. The thickness of each shell is 0.2 nm, which can sufficiently resolve spatial variations in the system while enclosing a statistically meaningful sample of water molecules. We identify each shell using its midpoint radial position, r , relative to the radial location of the CNT surface, R_c . We sort molecules based on the oxygen atom location, and position the shells such that the CNT surface is aligned with the shell boundary at $r = R_c$. The implementation of this layering scheme has no influence on the system dynamics. The shell-specific

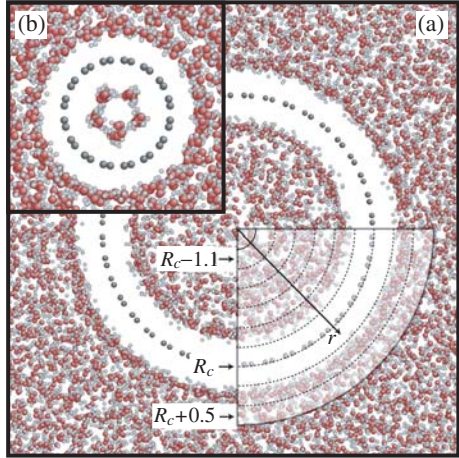


Figure 2: (color online) (a) Cropped axial snapshot of 2.8 nm CNT in water. Full simulation cell side length is 7.5 nm. The layering scheme used to analyze water near and within the CNT is also shown. Each layer has a thickness of 0.2 nm and is identified using the midpoint radial position, r . (b) Cropped axial snapshot of 1.1 nm CNT in water. Full cubic simulation cell side length is 5 nm. Both images are to the same scale and all numbers are in nm.

data presented throughout this report were then obtained by averaging the statistics of each shell over five data sets, with each set consisting of a 200 ps equilibration period followed by 250 ps of data collection.

III. Water Density

Although the water molecules are continually moving, the time-averaged number of molecules within each liquid layer is well defined. Far from the CNT, the average number of molecules in each layer is spatially uniform and corresponds to the bulk density of 1000 kg/m^3 . Closer to the CNT surface, as shown in Fig. 3, the unconfined water density is maximized at $r=R_c+0.3 \text{ nm}$, minimized at $r=R_c+0.5 \text{ nm}$, and slightly enhanced at $r=R_c+0.7 \text{ nm}$. The density profiles within the unconfined water near each CNT are indistinguishable from what we found near a flat graphene sheet, implying that surface curvature has no effect on the radial density profile outside the CNT. In agreement with our predictions, scanning tunneling microscopy measurements of water on graphite reveal a distinct and dense water layer beginning 0.25 nm from the carbon surface.²⁹ Our findings also agree with electronic structure calculations of water molecules near a flat graphite surface, which predict a water/graphite equilibrium separation distance of 0.32 nm.³⁰

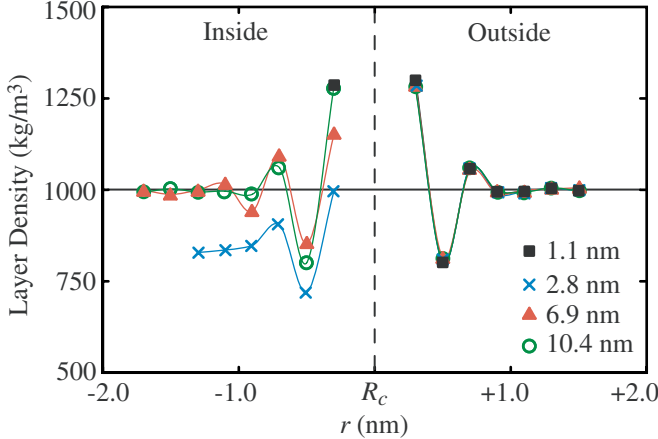


Figure 3: (color online) Water density inside and outside each CNT. The density profile in the unconfined water is invariant with CNT diameter and the same as that near a flat graphene sheet. The density profile in the confined water is a function of tube diameter. The inner-most layers for the 1.1 and 2.8 nm tubes are at $r=R_c-0.3$ nm and $r=R_c-1.3$ nm. Guidelines are added to highlight the minima and maxima.

Similar density variations have been experimentally observed near the krypton-graphite interface³¹ and predicted from MD simulation of liquid argon in a nanochannel.²⁸ This consistency suggests that although the current system includes electrostatic interactions, the density variations in the interfacial region are caused by the carbon-oxygen and oxygen-oxygen van der Waals interactions. At $r=R_c+0.3$ nm, the calculated carbon-oxygen potential energy due to LJ interactions is minimized, suggesting that the density maximum is indeed caused by oxygen atoms (and the associated water molecules) being drawn into an energetically favorable region near the carbon surface. At distances greater than $r=R_c+0.3$ nm, the carbon-oxygen LJ energy monotonically increases to zero and becomes too weak to directly influence water dynamics. Yet, the dense assembly of water molecules at $r=R_c+0.3$ nm extends the influence of the solid. At $r=R_c+0.5$ nm, 0.2 nm (one shell) beyond the water layer at $r=R_c+0.3$ nm, the calculated oxygen-oxygen interaction energy between water molecules is maximized. Thus, the dense layer at $r=R_c+0.3$ nm repels the molecules at $r=R_c+0.5$ nm, making the region energetically unfavorable and generating the density minimum seen in Fig. 3. The density enhancement at $r=R_c+0.7$ nm is then caused by attractive LJ interactions with the dense water layer at $r=R_c+0.3$ nm. This explanation seems reasonable given that the individual oxygen-oxygen LJ equilibrium separation distance, $2^{1/6}\sigma_{oo}$, is 0.36 nm.

Also presented in Fig. 3 is the density profile of the water confined inside each CNT. Unlike

the exterior density profiles, the radial distribution of confined fluid molecules is strongly related to tube size. Water confined within the 10.4 nm CNT behaves much like the outside water, with similar density oscillations and a bulk-like density of 1000 kg/m^3 recovered 1.0 nm from the solid surface. Inside the 6.9 nm tube, a bulk-like water density of 1000 kg/m^3 is also recovered at the tube centerline. The density variations penetrate further into the liquid than those in the exterior interface, however, suggesting that surface curvature influences molecular behavior within the confined region as the CNT diameter decreases below 10 nm.

Inside the 2.8 nm CNT, the equilibrium water density at the tube centerline is 840 kg/m^3 — significantly lower than the unconfined bulk density. Unlike in the larger tubes, where the 1 nm extent of surface effects is small compared to the tube diameter, the interface region within the 2.8 nm CNT is comparable to the tube diameter. The tube is too small to fully attenuate the influence of the solid and the confined water does not recover bulk properties. Thus, the behavior of water confined in a CNT becomes geometry dependent as the CNT diameter is decreased below 10 nm, consistent with the MD predictions of Koga and Tanaka for rectangular geometries⁸ and Maniwa *et al.* for CNTs.³² The water molecules inside the 1.1 nm CNT [see Fig. 2(b)] form a pentagon at $r=R_c-0.3 \text{ nm}$ with a density equivalent to that of the first exterior layer. Although some molecules diffuse across the channel centerline, the time-averaged number of particles outside this monolayer is very close to zero.

IV. Water molecule distribution

In addition to radial density variations, the distribution of water molecules around the CNT surface and along the tube axis varies with position. The water position probability distributions, $P_r(\theta, z)$, at $r=R_c+0.3 \text{ nm}$ and $r=R_c-0.3 \text{ nm}$ for the 6.9, 2.8, and 1.1 nm CNTs are shown in Figs. 4(a)-4(c). The surface shading indicates mass distribution. The carbon structure of each CNT at $r=R_c$ is also shown.

For all four nanotubes, water molecules at $r=R_c+0.3 \text{ nm}$ assume a pattered mass distribution which follows the hexagonal structure of the carbon surface. This non-uniform mass distribution agrees with the dynamic force microscopy measurements of Ashino *et al.*,³³ who found that the forces within the carbon honeycomb for a singled-walled CNT were 45% greater than those near the carbon atoms. They demonstrated that the strong interactions form a potential well centered within the carbon honeycomb structure shaped much like the circular distribution profiles presented

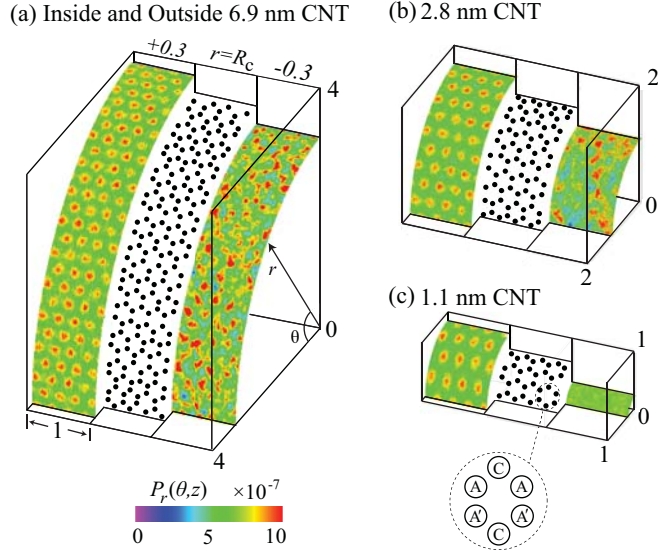


Figure 4: (color online)(a-c) Molecular distribution at $r=R_c+0.3$ nm, $r=R_c$, and $r=R_c-0.3$ nm for the 6.9, 2.8, and 1.1 nm CNTs. The mass distribution at $r=R_c+0.3$ nm is similar for all tubes. For the 10.4 nm CNT, this same pattern is present at both $r=R_c-0.3$ nm and $r=R_c+0.3$ nm. The distribution at $r=R_c-0.3$ nm for the 6.9, 2.8, and 1.1 nm CNTs becomes more uniform with decreasing CNT diameter. In frame (c), the detailed view identifies the circumferentially-aligned (C) and axially-aligned carbon atoms (A and A') that form the six-atom carbon honeycomb. All dimensions are in nm.

in Fig. 4. Their measured well-minimum is located 0.37 nm from the carbon surface, very close to the location of our predicted density maximum. Moreover, these authors conclude that van der Waals interactions are the dominate interatomic forces near the surface, supporting our earlier hypothesis.

In the confined region, $P_r(\theta, z)$ at $r=R_c-0.3$ nm becomes more uniform with decreasing CNT diameter. Inside the 10.4 nm CNT (not shown), molecules assume a distribution indistinguishable from that near the exterior interface, confirming that curvature effects within such large CNTs are negligible. Within the 6.9 nm CNT, the mass distribution likewise assumes a honeycomb structure following the CNT surface. Compared to the 10.4 nm CNT, however, the patterning in the 6.9 nm CNT is less prominent. Inside the 2.8 nm CNT, density enhancements are present near and within some carbon honeycombs while other potential wells remain unfilled. Finally, within the 1.1 nm CNT, the molecular positions are completely uncorrelated to the carbon structure.

These trends suggest that reducing the CNT diameter pinches the interior potential wells cen-

tered within the carbon honeycombs, thereby squeezing molecules out of the honeycomb structure and towards the CNT centerline. Unable to settle within the pinched potential well, the molecules at $r=R_c-0.3$ nm become more uniformly distributed with decreasing CNT diameter. This pinching mechanism also explains why the 10.4 nm and 6.9 nm CNTs, which both recover a bulk-like 1000 kg/m^3 density across the tube centerline, have different interior water density profiles: since fewer water molecules fill the pinched potential wells inside the 6.9 nm CNT honeycombs, the radial density at $r=R_c-0.3$ nm is lower than that inside the 10.4 nm CNT. Squeezed further from the solid surface, however, the influence of the molecules at $r=R_c-0.3$ nm near the 6.9 nm CNTs penetrates deeper into the confined fluid and extends the influence of the solid. Consistent with this idea, we have also found that with decreasing CNT diameter, the first peak of the carbon-oxygen radial distribution function inside the tube is located further from the carbon surface.

V. Water molecule orientation

To predict the influence of solid-liquid interactions on water molecule orientation, we calculate the unit dipole moment vector of all molecules with respect to the CNT surface normal. The vectors for all atoms in a given layer are then mapped onto a single unit sphere to form a layer-specific orientation distribution. In layers far from the surface, where interactions with the solid are fully attenuated, the molecular orientation distribution is uniform. At $r=R_c+0.3$ nm and $r=R_c-0.3$ nm, however, the molecules take on preferred orientations.

The orientation distribution map of water molecules at $r=R_c+0.3$ nm for the 6.9 nm CNT is shown in Fig. 5(a). Similar behavior is observed outside all four CNTs. Although all orientations are accessible to molecules in this layer, the molecules are most likely to point in one of three preferred directions. To understand this behavior, recall from Fig. 4 that water molecules are likely to reside in the potential well formed by the six-atom carbon honeycomb structure. As shown in Fig. 4(c), one pair of carbon atoms are axially-aligned and two pairs of carbon atoms are circumferentially-aligned. Although this symmetric arrangement generates a near circular potential well, water molecules within the potential well tend to point towards either a circumferentially-aligned carbon atom (C) or an axially-aligned carbon atom (A or A').

The orientation distribution maps of water molecules at $r=R_c-0.3$ nm for the 6.9, 2.8, and 1.1 nm CNT are shown in Figs. 5(a)- 5(c). Although not presented here, we note that the molecules at $r=R_c-0.3$ nm for the 10.4 nm nanotube orient like those at $r=R_c+0.3$ nm but mirrored towards

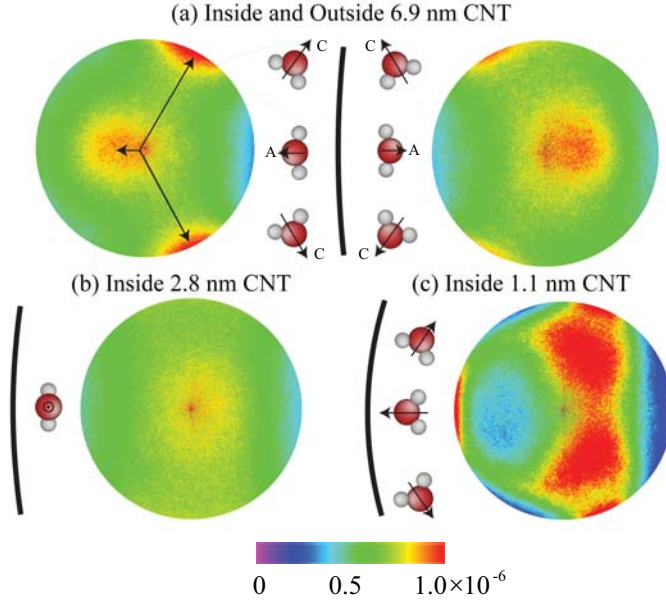


Figure 5: (color online) (a) Orientation distribution spheres at $r=R_c+0.3$ and $r=R_c-0.3$ nm for the 6.9 nm CNT. The projected length of the unit dipole moment vector, as printed in the figure, indicates the degree of rotation out of the plane of the page. Molecules are biased towards either an axially-aligned carbon atom (A) or a circumferentially-aligned carbon atom (C), as highlighted by the orientation distribution and the three water molecules beside the sphere. (b) Orientation distribution at $r=R_c-0.3$ nm near the 2.8 nm CNT. A single preferred orientation points normal to (in or out of) the page. (c) Distribution at $r=R_c-0.3$ nm near the 1.1 nm CNT. The water molecules form a pentagonal structure, resulting in two preferred orientations pointing away from the surface. A third preferred orientation points towards the CNT surface but is unbiased towards any particular axially or circumferentially-aligned carbon atom.

the CNT surface. At $r=R_c-0.3$ nm for the 6.9 nm CNT, the water molecules are still likely to align with the CNT centerline axis but, compared to the 10.4 nm CNT, less likely to point towards a specific circumferentially-aligned carbon atom. This trend continues in the 2.8 nm CNT, where water molecules at $r=R_c-0.3$ nm remain aligned with the CNT centerline axis, but have no affinity towards any particular circumferentially-aligned carbon atom. These correlations between orientation distribution and CNT diameter support the squeezing mechanism discussed earlier. As an increasing fraction of water molecules are squeezed out of the carbon honeycomb potential well, distinct interactions with the circumferentially-aligned carbon pair become less pronounced. Thus, with decreasing CNT diameter, interactions between water and specific circumferentially-aligned

carbon atoms are less distinct and water molecules are instead spread over an increasing range of orientations. A preferred orientation remains in the direction of the axially-aligned carbon atoms, however, since these atomic positions are unaffected by surface curvature. For the 1.1 nm CNT, the molecules are fully squeezed from the surface potential wells and two preferred orientations point away from the carbon surface. The orientation distribution is now governed by water-water interactions, forming the pentagonal arrangement illustrated in Fig. 2(b) and manifested in the orientation distribution. Unique molecular orientation distributions inside sub-2-nm CNTs were also reported by Koga *et al.*³⁴

VI. Summary and conclusion

We have investigated the effect of tube diameter on the density, molecular distribution, and molecular orientation of water inside and outside single-walled CNTs. As presented in Figs. 3 and 4, the density of unconfined water molecules is enhanced and the molecular distribution is non-uniform near the carbon surface. This behavior is caused by water molecules moving to low-energy potential wells formed near the hexagonal carbon surface. The behavior of unconfined water molecules is invariant with CNT diameter. Inside the tube, however, curvature effects influence the molecular density and distribution near the CNT wall. The curved surface pinches the low-energy potential wells, thereby squeezing water molecules away from the carbon surface and decreasing the liquid density.

In addition to density and molecular distribution, interactions with the CNT influence the orientation of water molecules near the carbon surface. As presented in Fig. 5, the unconfined water molecules close to a CNT of any diameter are likely to point towards either a circumferentially or axially-aligned carbon atom. Water molecules confined within the 10.4 and 6.9 nm CNT orient much like unconfined water molecules. Inside the 2.8 nm CNT, where surface curvature effects are more relevant, water molecules are only likely to point towards axially-aligned carbon atoms. Inside the 1.1 nm CNT, the molecular orientation is governed by water-water interactions and molecules have no affinity towards any particular carbon atom.

Tersoff and Ruoff predicted that van der Waals attraction between CNTs with diameters greater than 2.5 nm would cause the tubes to flatten against each other and form hexagonal cross-sections.³⁵ López *et al.* have observed this so-called “polygonization” experimentally.³⁶ Inside our 2.8 nm CNT, where the water molecules do not recover bulk-like properties, polygonization may influence

the behavior of the confined fluid. Inside larger tubes, where bulk-like properties are recovered, polygonization is unlikely to have an effect. Such bundling is likely to influence the behavior of water molecules in the interstitial region between two or more clustered CNTs.

The reduced influence of solid-water interactions on molecular orientation and distribution as the tube diameter gets smaller may be responsible for the high mass flow rates reported for water through 0.81 nm CNTs.^{5,9} This behavior also suggests that thermal energy exchange between a CNT and surrounding fluid may be affected by tube diameter.³⁷

References

- [1] G. Gruner, Anal. Bioanal. Chem **384**, 322 (2006).
- [2] Y. Yun *et al.*, Proc. of SPIE, Ed. V. K. Varadan **6528**, 65280T (2007).
- [3] J. Li, C. Papadopoulos, and J. Xu, Nature **402**, 253 (1999).
- [4] A. I. Skouidas, D. M. Ackerman J. K. Johnson, and D. S. Sholl, Phys. Rev. Lett. **89**, 185901 (2002).
- [5] J. K. Holt *et al.*, Science **312**, 1034 (2006).
- [6] M. Shim, N. W. S. Kam, R. J. Chen, Y. Li, and H. Dai, Nano Lett **2**, 285 (2002).
- [7] J. Martí and M. C. Gordillo, Phys. Rev. E **64**, 021504 (2001).
- [8] K. Koga and H. Tanaka, J. Chem. Phys. **122**, 104711 (2005).
- [9] G. Hummer, J. C. Rasaiah, and J. P. Noworyta, Nature **414**, 188-190 (2001).
- [10] E. S. Landry, S. Mikkilineni, M. Paharia, and A. J. H. McGaughey, To appear in J. App. Phys..
- [11] M. P. Allen and D. J. Tildesley, *Computer Simulation of Liquids* (Oxford University Press, New York, 1987).
- [12] R. S. Taylor, L. X. Dang, and B. C. Garrett, J. Phys. Chem. **100**, 11720 (1996).
- [13] J. H. Walther, R. L. Jaffe, T. Halicioglu, and P. Koumoutsakos, J. Phys. Chem. B **107**, 1345 (2003).
- [14] N. Choudhury, J. Phys. Chem. C **111**, 2565 (2007).
- [15] E. M. Kotsalis, J. H. Walther, and P. Koumoutsakos, Int. J. Multiphas. Flow **30**, 995 (2004).
- [16] I. Hanasaki and A. Nakatani, J. Chem. Phys. **124**, 144708 (2006).
- [17] J. Zou, B. Ji, X.-Q. Feng, and H. Gao, Small **2**, 1348 (2006).
- [18] Y. Maniwa *et al.*, Chem. Phys. Lett. **401**, 534 (2005).
- [19] M. W. Mahoney and W. L. Jorgensen, J. Chem. Phys. **112**, 8910 (2000).

- [20] M. Lísal, J. Kolafa, and I. Nezbeda, *J. Chem. Phys.* **117**, 8892 (2002).
- [21] D. J. Griffiths, *Introduction to Electrodynamics, 3th Edition* (Prentice Hall, New Jersey, 1999).
- [22] M. W. Mahoney and W. L. Jorgensen, *J. Chem. Phys.* **114**, 363 (2001).
- [23] W. L. Jorgensen and J. Tirado-Rives, *P. Natl. A. Sci. USA* **102**, 6665 (2005).
- [24] T. Werder, J. H. Walther, R. L. Jaffe, T. Halicioglu, and P. Koumoutsakos, *J. Phys. Chem. B* **107**, 1345 (2003).
- [25] A. H. Barber, S. R. Cohon, and H. D. Wagner, *Phys. Rev. B* **71**, 115443 (2005).
- [26] R. L. Jaffe, P. Gonnet, T. Werder, J. H. Walther, and P. Koumoutsakos, *Mol. Simulat.* **30**, 205 (2004).
- [27] F. Moulin, M. Devel, and S. Picaud, *Phys. Rev. B* **71**, 165401 (2005).
- [28] J. A. Thomas and A. J. H. McGaughey, *J. Chem. Phys.* **126**, 034707 (2007).
- [29] G. Nagy, *J. Electroanal. Chem.* **409**, 19 (1996).
- [30] D. Feller and K. D. Jordan, *J. Phys. Chem. A* **104**, 9971 (2000).
- [31] R. F. Hainsey, R. Gangwar, J. D. Shindler, and R. M. Suter, *Phys. Rev. B* **44**, 3365 (1991).
- [32] Y. Maniwa, H. Kataura, M. Abe, S. Suzuki, Y. Achiba, H. Kira and K. Matsuda, *J. Phys. Soc. Jpn.* **71**, 2863 (2002).
- [33] M. Ashino, A. Schwarz, T. Behnke, and R. Wiesendanger, *Phys. Rev. Lett.* **93**, 136101 (2004).
- [34] K. Koga, G. T. Gao, H. Tanaka and X. C. Zeng, *Nature* **412**, 802 (2001).
- [35] J. Tersoff and R. S. Rubio, *Phys. Rev. Lett.* **76**, 676 (1994).
- [36] M. J. López, A. Rubio, J. A. Alonso, L.-C. Qin, and S. Iijima, *Phys. Rev. Lett.* **86**, 3056 (2001).
- [37] M. Shenogin, L. Xue, R. Ozisik, P. Kebelinski, and D. G. Cahill, *J. App. Phys.* **95**, 8136 (2004).

Fig. 1. (color online) Intermolecular force versus oxygen separation distance between two water molecules in an equilibrated simulation of 512 molecules at a temperature of 298 K and a pressure of 1 atm. The gray envelope represents the range of forces predicted at each separation distance. The solid line is the mean force at each distance. Inset: Force envelope and mean force at separation distances greater than 0.7 nm. At these separations, the force envelope decays as $1/(r_{OO})^4$, characteristic of a permanent dipole-permanent dipole interaction. The mean effective force is related to the oxygen-oxygen LJ interactions and decays as $1/(r_{OO})^7$.

Fig. 2. (color online) (a) Cropped axial snapshot of 2.8 nm CNT in water. Full simulation cell side length is 7.5 nm. The layering scheme used to analyze water near and within the CNT is also shown. Each layer has a thickness of 0.2 nm and is identified using the midpoint radial position, r . (b) Cropped axial snapshot of 1.1 nm CNT in water. Full cubic simulation cell side length is 5 nm. Both images are to the same scale and all numbers are in nm.

Fig. 3. (color online) Water density inside and outside each CNT. The density profile in the unconfined water is invariant with CNT diameter and the same as that near a flat graphene sheet. The density profile in the confined water is a function of tube diameter. The inner-most layers for the 1.1 and 2.8 nm tubes are at $r=R_c-0.3$ nm and $r=R_c-1.3$ nm. Guidelines are added to highlight the minima and maxima.

Fig. 4. (color online)(a-c) Molecular distribution at $r=R_c+0.3$ nm, $r=R_c$, and $r=R_c-0.3$ nm for the 6.9, 2.8, and 1.1 nm CNTs. The mass distribution at $r=R_c+0.3$ nm is similar for all tubes. For the 10.4 nm CNT, this same pattern is present at both $r=R_c-0.3$ nm and $r=R_c+0.3$ nm. The distribution at $r=R_c-0.3$ nm for the 6.9, 2.8, and 1.1 nm CNTs becomes more uniform with decreasing CNT diameter. In frame (c), the detailed view identifies the circumferentially-aligned (C) and axially-aligned carbon atoms (A and A') that form the six-atom carbon honeycomb. All dimensions are in nm.

Fig. 5. (color online) (a) Orientation distribution spheres at $r=R_c+0.3$ and $r=R_c-0.3$ nm for the 6.9 nm CNT. The projected length of the unit dipole moment vector, as printed in the figure, indicates the degree of rotation out of the plane of the page. Molecules are biased towards either an axially-aligned carbon atom (A) or a circumferentially-aligned carbon atom (C), as highlighted by the orientation distribution and the three water molecules beside the sphere. (b) Orientation distribution at $r=R_c-0.3$ nm near the 2.8 nm CNT. A single preferred orientation points normal to (in or out of) the page. (c) Distribution at $r=R_c-0.3$ nm near the 1.1 nm CNT. The water molecules form a pentagonal structure, resulting in two preferred orientations pointing away from the surface. A third preferred orientation points towards the CNT surface but is unbiased towards any particular axially or circumferentially-aligned carbon atom.

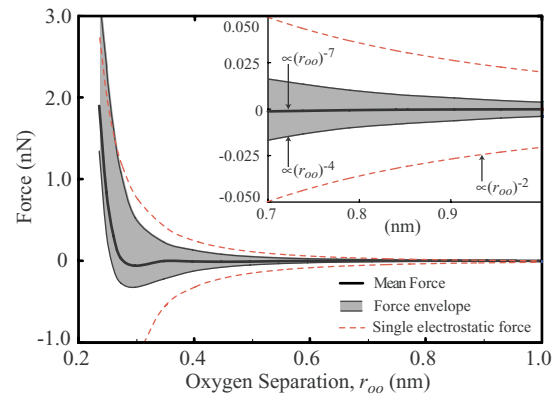


Figure 1

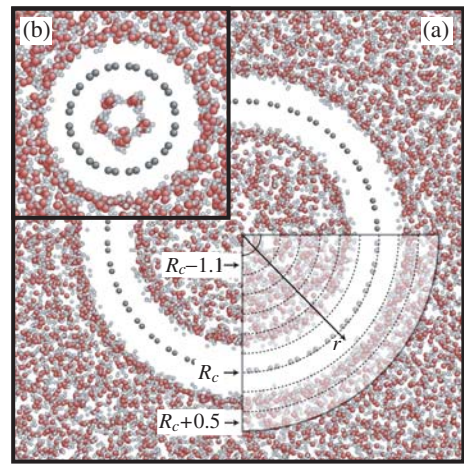


Figure 2

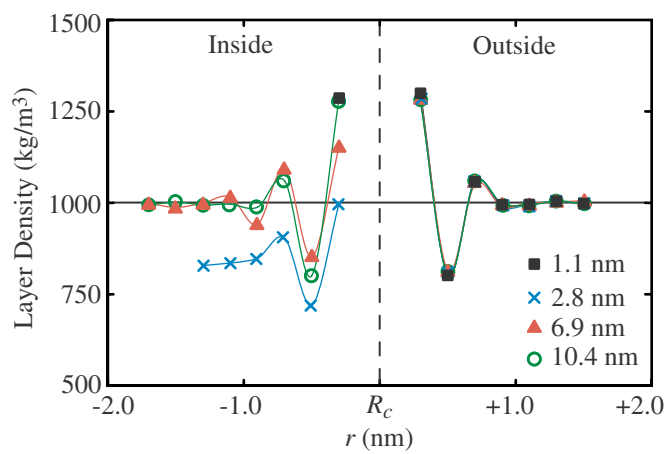


Figure 3

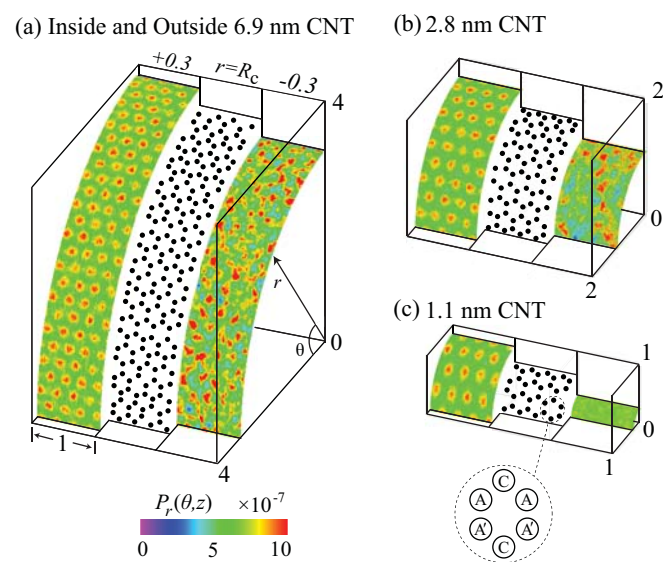


Figure 4

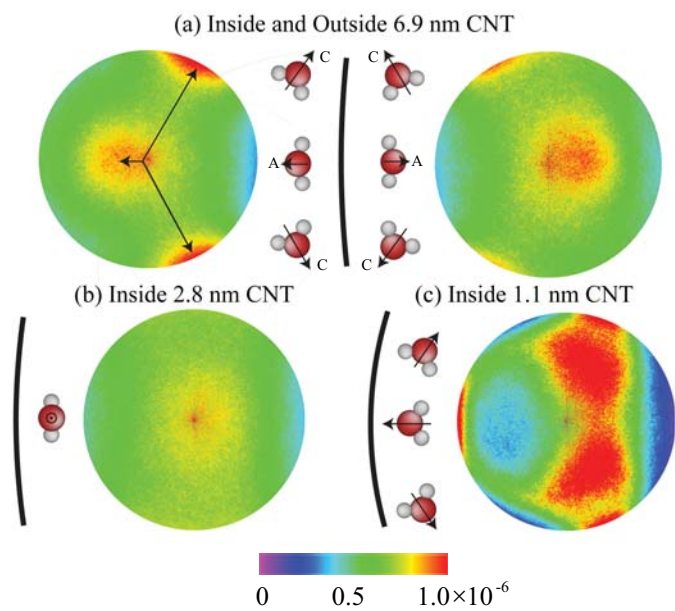


Figure 5